Numerical simulation of a confined cavitating gas bubble driven by ultrasound

Jacqueline Mifsud,[1] Duncan A. Lockerby,[1] Yongmann M. Chung,[1] and Gordon Jones[2]
[1)]*School of Engineering, University of Warwick, Coventry CV4 7AL, United Kingdom*
[2)]*Waters Corporation, Stamford Avenue, Wilmslow SK9 4AX, United Kingdom*

(*gordon_jones@waters.com)

(*y.m.chung@warwick.ac.uk)

(*duncan.lockerby@warwick.ac.uk)

(*Author to whom correspondence should be addressed: j.mifsud@warwick.ac.uk)

(Dated: 20 November 2021)

This work investigates the flow disturbance generated by an ultrasonically-driven gas bubble confined in a narrow gap over one acoustic cycle. Here, we provide a more accurate representation of ultrasonic cleaning by implementing a Volume-of-Fluid model in OpenFOAM that simulates the ultrasound as a sinusoidally time-varying pressure boundary condition. A modified Rayleigh-Plesset equation is solved to select an acoustic forcing that instigates bubble collapse. Simulations reveal the interaction between the inflow from the acoustic forcing and the flow deflected by the confining walls intensifies the strength of the self-piercing micro-jet(s), and consequently of the unsteady boundary layer flow, compared to the traditional collapse near a single rigid wall. Depending on the gap height and the position of bubble inception inside the gap, three distinct collapse regimes involving dual-jets or directed-jets are identified, each resulting in a different shear-stress footprint on the confining boundaries. Plots of the spatio-temporal evolution of the shear flow (that is difficult to measure experimentally) reveal peak shear-stress magnitudes at collapse that are double those reported for an undriven laser-induced bubble in similar geometric confinement. This twofold increase is attributed to the ultrasonic signal driving the collapse. Surprisingly, in our simulations we have not encountered a transferred-jet regime previously observed for an unforced bubble collapsing in a similar configuration. This unexpected finding highlights the different physics involved in modelling acoustically-driven bubbles compared to the conventional laser-induced bubbles used in experiments.

I. INTRODUCTION

Cavitation is an established topic in fluid dynamics, having been studied for more than a century. The collapse stage is rich in phenomena including a high-speed jet flow, shock wave emission and a strong localised shear flow as the jet spreads along the boundary, amongst others.[1] Repeated bubble collapse near the same location can have serious destructive effects on material surfaces, causing erosion and subsequent loss of performance in turbomachinery or marine propulsion systems;[2] but it can also be exploited for beneficial purposes.[3–5] In fact, although cavitation was first investigated due to its disruptive effects,[2] it is nowadays at the core of several practical applications including: i) microfluidic (lab-on-chip) devices;[6] ii) medical treatments;[3,7] and iii) ultrasonic cleaning of surfaces.[8,9] Its widespread utilization in various industries owes to its ability to concentrate massive amounts of energy into small volumes.[10] In acoustic cavitation in particular, as the bubble oscillates it absorbs energy from the ultrasound that is transferred into the momentum of a high-speed liquid jet during its collapse. The collapse of an acoustically-driven bubble therefore tends to be more violent than in the absence of the ultrasound.[11]

Of particular interest in this study is the ultrasonic cleaning application, a process used to remove surface contamination, manufacturing residue (e.g. particulate debris), and biofilms in various contexts. In a clinical setting, shape-oscillating or 'dancing' bubbles emanating from dental ultrasonic scalers are used to remove bacterial biofilms on the surface of dental implants or teeth.[12,13] Techniques for delicate cleaning are highly desirable since damage to the surface induces roughness that may exacerbate plaque build-up and prevent the complete removal of bacterial biofilms. Several

studies have demonstrated that acoustic cavitation can clean intricate patterns and reach into deeper geometries (e.g., crevices or surface roughness) that would otherwise remain uncleaned if using other contemporary methods.[13–17] Albeit being widely utilized, the ultrasonic cleaning process is still not entirely understood. The relation between bubble-induced flow and the cleaning action has been evidenced in multiple studies,[18–21] and it is now accepted that the cleaning action is a combination of the array of phenomena associated with cavitation bubble collapse and not the ultrasound itself. As a matter of fact, unforced laser-induced cavitation bubbles also have the potential to clean surfaces.[18] The flow features span across time and length scales making their experimental visualization using high-speed cameras challenging and at the limit of current state-of-the-art capabilities.[22] Besides, experimental measurements of physical quantities at such small scales is inherently difficult. For instance, the strong shear flow along the boundary is one of the main mechanisms responsible for cleaning, but only a couple of experimental techniques have been successful in measuring its strength.[21,23] On the other hand, using Computational Fluid Dynamics (CFD) simulation it is possible to obtain a more comprehensive understanding of the mechanisms responsible for cleaning since the full details of the flow-field evolution are computed and there are also no limits on the location and number of measurements that can be made.

In many ultrasonic cleaning processes, for instance in the cleaning of silicon wafers and computer components,[1,17] the acoustically-driven cavitation activity takes place in highly confined spaces. Boundaries are sources of bubble deformation and typically induce self-piercing jets whose strength and direction is highly influenced by the rigidity (elasticity) of the boundary and its proximity.[24,25] Recent studies for an unforced bubble collapsing in a narrow gap of variable height have found an intensification of the jet velocity,[26] suggesting that this may enhance the shear stresses on boundaries and therefore the cleaning action compared to the case of a single rigid wall.[27] The oscillation of a bubble in between two parallel plates has a long-standing interest in the research community.[28] Theoretical descriptions of this problem date back to 1980 by Shima and Sato who had already identified that the collapse time between two opposing walls is longer than for a bubble collapsing near a single rigid wall and the importance of viscosity on the dynamics of the confined bubble. Experimental studies confirm these theoretical predictions and demonstrate the rich array of dynamics (necking, splitting and jetting) associated with this configuration.[30–36] Although a number of computational studies have considered the behaviour of cavitation bubbles in confinement,[26,37–42] only a handful of these consider the viscosity and investigate the bubble-induced shear stress on confining surfaces.[27,43] Furthermore, none of these studies has considered the acoustically-driven collapse of a bubble, where the shear rates observed are dependent on the strength of the driven acoustic field.

Acoustically-driven bubbles in tubular geometries have been investigated due to their relevance in the biomedical field,[44–46] where forcing frequencies are typically much higher ($\sim$ MHz) compared to ultrasonic cleaning ($\sim$ kHz). Kilohertz frequencies have only been considered in computational studies for collapse near a single rigid boundary.[47–50] This is a mature problem especially for unforced laser-induced bubbles, i.e. starting from a small volume at high pressure ($\sim$ 1000 bar) to capture the explosive growth[51] typically observed in experiments involving optic cavitation. In comparison, experimental and numerical investigations of an isolated acoustic cavitation bubble are still scarce. Boyd and Becker[49] have considered the acoustically-driven growth and collapse of a gas microbubble in the vicinity of a single rigid wall. The acoustic forcing was modelled through a moving boundary representative of the transducer face. In some cases, including an earlier study by Boyd and Becker[48], the growth stage of the bubble is ignored entirely and only the collapse stage is modelled.[52] This requires assuming a perfectly spherical bubble at maximum expansion; an approximation that becomes increasingly inaccurate for decreasing bubble-wall separations and one that is inconsistent with experimental observations.[24,53] While the acoustic signal has been considered by Boyd and Becker[49], surface tension and viscosity effects have been ignored. Consequently, the unsteady boundary layer flow induced by the acoustic bubble oscillation cannot be captured; making it impossible to investigate mechanisms such as shear forces that are relevant to ultrasonic cleaning. Furthermore, the importance of viscous effects on jet formation and evolution has already been demonstrated for laser-induced bubbles,[54,55] suggesting that consideration of viscosity is also important for acoustically-driven bubbles and can no longer be overlooked. Denner, Evrard, and van Wachem[50] have improved upon this by developing an in-house volume-of-fluid (VOF) code that accounts for liquid compressibility as well as viscous effects, but still neglects surface tension.

While the surface tension can often be safely neglected for micron-size bubbles and much larger bubbles (e.g. underwater explosion bubbles[56,57]), its pressure contribution becomes increasingly important for decreasing bubble sizes R_n (typically sub-micron bubble sizes) according to the (inverse) scaling factor $2\sigma/R_n$ in the Young Laplace equation. Meanwhile, the inclusion of viscosity in Ref. 50 enabled the prediction of wall shear stresses, with peak magnitudes in excess of 100 kPa at bubble collapse.

In contrast, the VOF algorithm proposed in this study considers both surface tension and viscosity effects as well as the nonlinear compressibility of the liquid, thus providing a comprehensive model for acoustic cavitation dynamics. Our scope is to offer an efficient, stable algorithm for acoustic cavitation simulation that is relatively easy to implement in OpenFOAM. The confined geometry considered combined with the acoustic forcing offers a more realistic representation of practical applications such as ultrasonic cleaning where the acoustic bubble activity is known to take place in highly confined spaces. Additionally, the inclusion of viscosity in the proposed VOF algorithm has enabled the quantification of the *acoustic* bubble-induced shear forces on the confining boundaries to provide an estimate of the cleaning potential. The method also supports various specialized discretization schemes that offer mesh non-orthogonality and skewness corrections, allowing for more flexibility in the mesh configurations that can be used besides strictly rectilinear grids.

The manuscript is organized as follows: Sec. II introduces the theoretical bubble model and the corresponding CFD methodology. In Sec. III, a verification and validation study are presented to assess the suitability of the numerical model for acoustic cavitation simulation. The main results of a parametric study on confined acoustic cavitation are presented in Sec. IV. The discussion in Sec. V focusses on the induced wall shear stress due to its relevance in cleaning applications. The conclusions and key findings of this study are summarised in Sec. VI.

II. CFD METHODOLOGY

The pressure-based interfacial flow solver `compressibleInterFoam` available within the open-source framework of OpenFOAM is adopted for the simulation. It involves a compressive algebraic VOF method; a one-fluid formulation that is computationally efficient since no geometric reconstruction of the interface is required and fluxes are simply computed algebraically.[58] In VOF, the interface is implicitly captured on a fixed grid, appearing and disappearing naturally.[59] As a result, drastic topology changes are not an issue, with the merging and break-up of interfacial sctructures usually dictated only by the grid resolution[60] without the need for artificial manipulation of the interface often required by boundary-fitted methods.[61] This makes the algebraic-VOF technique relatively straightforward to generalize to 3D and parallelize for use on computer clusters. Usage of this VOF solver for bubble dynamics problems has become increasingly prevalent within the research community in recent years.[27,38,55,56,62–68] However, only a handful of these previous works considered the acoustic forcing.[69,70]

A. Governing Equations

Equations of motion are formulated for a single-fluid having a common velocity field $\mathbf{U}(x,t)$, pressure field $p(x,t)$ and density field $\rho(x,t)$ defined on a fixed (Eulerian) grid. In the following equations $\nabla\cdot$ denotes the divergence and ∇ the gradient operator. Subscripts g and l distinguish between properties pertaining to the gas and liquid phases, respectively. The solution of the Navier-Stokes equations is required:

$$\frac{\partial \rho}{\partial t} + \nabla \cdot (\rho \mathbf{U}) = 0\,, \tag{1}$$

$$\frac{\partial (\rho \mathbf{U})}{\partial t} + \nabla \cdot (\rho \mathbf{U}\mathbf{U}) = -\nabla p + \nabla \cdot \mathbb{T} + f_\sigma\,, \tag{2}$$

where f_σ is the surface tension force modelled according to the Continuum Surface Force (CSF) method of Brackbill[71] and $\mathbb{T}$ is the viscous stress tensor defined as:

$$\mathbb{T} = \mu \left(\nabla \mathbf{U} + (\nabla \mathbf{U})^{\mathrm{T}} - \frac{2}{3}(\nabla \cdot \mathbf{U})\mathbb{I} \right),$$

in which $\mathbb{I}$ is the unit tensor. In VOF, an additional transport equation introduced for the volume fraction α:

$$\frac{\partial \alpha_l}{\partial t} + \nabla \cdot (\alpha_l \mathbf{U}) + \nabla \cdot (\mathbf{U}_r \alpha_l \alpha_g) = \alpha_l \alpha_g \left(\frac{\psi_g}{\rho_g} - \frac{\psi_l}{\rho_l} \right) \left(\frac{\mathrm{D}p}{\mathrm{D}t} \right) + \alpha_l \nabla \cdot \mathbf{U}, \tag{3}$$

The fluid type is identified based on the value of the volume fraction, α, in each computational cell:

$$\alpha_l = \begin{cases} 0, & \text{gas}, \\ 1, & \text{liquid}, \\ 0 < \alpha_l < 1, & \text{interface}. \end{cases}$$

In Eq. (3), ψ is the nonlinear compressibility defined as $\psi_i = (d\rho/dp)_i$ and can be derived from the relevant equation of state (EoS) (see Sec. II B). Inclusion of compressibility is required to capture weak shock waves in the liquid that can originate during the violent collapse of the cavitation bubble. The third term on the left-hand side (LHS) of Eq. (3) is an artificial compression term that helps counteract diffusion of the interface to preserve its sharpness.[72] It only acts in the interface region where $\alpha_l \alpha_g > 0$ and involves a relative velocity $\mathbf{U}_r$ acting normal to the interface between the two fluids.[73] The relative velocity can be interpolated to the face centers f of a computational cell with nodal velocity $\mathbf{U}_r$ to obtain $\mathbf{U}_{r,f}$ as:

$$\mathbf{U}_{r,f} = c_\alpha \frac{|\phi_f|}{|S_f|} \hat{n}, \tag{4}$$

where ϕ_f, S_f, c_α and $\hat{n}$ represent the velocity flux, the cell surface area vector, an adjustable compression factor and a unit vector acting normal to the interface respectively.[73–76] Here the value of c_α is set to unity for moderate compression.[75] The third term on the LHS of Eq. (3) is discretized using a specialised `interfaceCompression` scheme. Eq. 3 is solved semi-implicitly with the MULES[77] algorithm for several sub-cycles within one time-step.[78,79] Combined with compressive interface-capturing, MULES guarantees the boundedness of $\alpha \in [0,1]$ and maintains interface sharpness.[80,81] The first term on the right-hand side (RHS) of Eq. (3) represents the compressibility at the bubble-liquid interface[62,64] where the pre-factor $\alpha_l \alpha_g \neq 0$. This term is derived from the continuity equation: $(\alpha_l \psi_l/\rho_l + \alpha_g \psi_g/\rho_g)\,\mathrm{D}p/\mathrm{D}t + \nabla \cdot \mathbf{U} = 0$ as shown in Ref. 76 and can be a source of numerical instability. Particularly, in situations where $\mathrm{D}p/\mathrm{D}t$ assumes large values ($> 10^{14}\,\mathrm{Pa/s}$ in Koch *et al.*[62]), the liquid volume fraction α_l may decrease, resulting in the non-physical formation of artificial gas-filled regions in the liquid surrounding the bubble. In the simulations presented in this work, these issues were not encountered, but the interested reader may refer to Ref. 62 for a visual example of this instability and a tried-and-tested circumvention.

Temporal derivatives are discretized using an implicit `Euler` scheme which is first-order accurate but diffusive. Use of higher-order temporal schemes (e.g. backward Euler) with the current `compressibleInterFoam` solver is not recommended for this kind of problem, since strong discontinuities (e.g. shock waves) exist which may cause numerical errors and unwanted oscillations that compromise solution stability. The convective terms in the momentum equation (Eq. (2)) and in the transport equation for α (Eq. (3)) are discretized using a second-order upwind scheme and a second-order van Leer scheme, respectively. Other terms are discretized using a second-order `Gauss linear` scheme (central differencing) with provisions for mesh non-orthogonality and skewness as required. Appendix A provides a summary of the typical discretization schemes that were used to obtain the results in the remainder of this work. The pressure-velocity coupling is handled by the Pressure Implicit Splitting of Operators (PISO) algorithm.[62,75] An adaptive time-stepping algorithm controls the time-step size according to a maximum Courant number of 0.1. All simulation results in this study have been obtained using OpenFOAM v5.

B. Barotropic closure

The presented system of governing equations (Eqs. (1), (2), and (3)) is closed by the equations of state (EoS) for the respective phases. The barotropic EoS are chosen such that the density of each phase is only a function of the (absolute) pressure, $\rho_i(p)$, in lieu of solving an energy equation.[57] The pressure p and density ρ_l of the liquid are related through the Tait equation of state:[82]

$$\rho_l = \rho_{0,l}\left(\frac{p+B}{p_0+B}\right)^{\frac{1}{\eta}}, \tag{5}$$

where $\rho_{0,l}$ and p_0 are the density and pressure of the liquid at atmospheric conditions, respectively. The Tait exponent $\gamma_l = 7$ and the Tait pressure $B = 331\,\mathrm{MPa}$.[83] Similarly, the pressure p and density ρ_g of the gas are related through the polytropic equation of state:

$$\rho_g = \rho_{0,g}\left(\frac{p}{p_0}\right)^{\frac{1}{\gamma_g}}, \tag{6}$$

where $\rho_{0,g}$ and p_0 are the density and pressure of the gas (air) inside the bubble at atmospheric conditions, and the exponent $\gamma_g = 1.4$ is the specific heat ratio for air. The thermophysical properties are those for water as a liquid and air as gas at atmospheric conditions as summarised in Table I, together with the corresponding values. The physical properties of the equivalent fluid can then be averaged as follows:

$$\rho = \alpha_l\rho_l + (1-\alpha_l)\rho_g\,, \tag{7}$$

$$\mu = \alpha_l\mu_l + (1-\alpha_l)\mu_g\,. \tag{8}$$

All simulations in this work are conducted in axisymmetry to alleviate some of the computational cost of the problem. Note that, an axisymmetric simulation in OpenFOAM requires the construction of a 3D computational wedge domain, similar to that constructed in Ref. 62, for instance.

TABLE I. Summary of fluid properties used in the simulations.

Parameter	Symbol	Value
Surface tension [N/m]	σ	0.072
Bubble (air)		
Polytropic exponent	γ_g	1.4
Dynamic viscosity [Pa·s]	μ_g	1.84×10^{-5}
Reference density [kg/m^3]	$\rho_{0,g}$	1
Reference pressure [Pa]	$p_{0,g}$	1×10^5
Liquid (water)		
Tait exponent	γ_l	7
Dynamic viscosity [Pa·s]	μ_l	1×10^{-3}
Reference density [kg/m^3]	$\rho_{0,l}$	1000
Reference pressure [Pa]	$p_{0,l}$	1×10^5
Tait pressure [Pa]	B	331×10^6

C. Standard Rayleigh-Plesset Model

Model equations for a cavitation bubble can be formulated in terms of various parameters of the surrounding liquid and the bubble contents.[84] Evaporation and condensation are considered fast processes with respect to the timescale of bubble oscillation and therefore we can assume the bubble

contains only gas without any vapour. The mass of the microbubbles considered is too small for buoyancy to have an observable effect at these timescales. The most commonly used nonlinear equation of motion describing the oscillation of a spherical bubble in an infinite volume of liquid is the Rayleigh-Plesset Equation (RPE),[85] expressing the bubble radius as the dynamic parameter, $R = R(t)$, that varies based on the conditions of the gas and liquid. In its standard (unconfined) form, the RPE for an equilibrium radius R_n is:

$$R\ddot{R} + \frac{3}{2}\dot{R}^2 = \frac{1}{\rho_l}\left[p_{g,n}\left(\frac{R_n}{R}\right)^{3\gamma_g} - \frac{2\sigma}{R} - \frac{4\mu_l}{R}\dot{R} - p_\infty\right], \tag{9}$$

where $\dot{R} = \mathrm{d}R/\mathrm{d}t$ and $\ddot{R} = \mathrm{d}^2R/\mathrm{d}t^2$. In Eq. (9) the pressure balance at equilibrium, $p_{g,n}$, is defined by the Young-Laplace law:[84,86]

$$p_{g,n} = \frac{2\sigma}{R_n} + p_0, \tag{10}$$

where $p_{g,n}$ and p_0 are the equilibrium gas pressure inside the bubble and the static pressure, respectively. The pressure at the far-field, $p_\infty = p_0 \pm p(t)$, consists of static, p_0, and time-varying, $p(t)$, pressure contributions; where $p(t) = \pm\, p_{ac}\sin(2\pi f_{ac}t)$ varies sinusoidally with frequency f_{ac} (Hz) and acoustic pressure amplitude p_{ac} (Pa). A numerical approximation to Eq. (9) is obtained using an ordinary differential equation (ODE) solver in MATLAB.[87] From hereon, Eq. (9) for an unconfined bubble will be referred to as the *standard* RPE.

III. MODEL VERIFICATION AND VALIDATION

A. Spherical bubble oscillation: Forced Rayleigh Collapse

To assess the ability of the proposed VOF model in capturing the bubble's expansion and collapse in response to a time-varying pressure boundary condition (BC) imposed at the far-field, we model the spherical collapse in an unbounded liquid, known as the Rayleigh collapse. The computed bubble radius history is compared with the experimental data of Rodríguez-Rodríguez, Casado-Chacón, and Fuster[88]. This case has also been numerically simulated using a Coupled Level-Set Volume-Of-Fluid (CLSVOF) method by Chakraborty[83]. Therefore, this is an excellent verification exercise because it allows for a comparison of the present model with experimental results,[88] numerical solution to the analytical RPE in Eq. (9), as well as the computational results from another numerical method.[83]

1. Boundary and initial conditions

The bubble having equilibrium size of $R_n = 180\,\mu$m is initialised in a quiescent liquid. The corresponding bubble pressure $p_B = p_{g,n}$ is determined from Eq. (10). The fluid parameters in this section vary from those in Table I to match those in the experiments.[88] Specifically, the gas inside the bubble is carbon-dioxide (CO_2) with the corresponding CO_2-water surface tension coefficient $\sigma = 0.0434\,\mathrm{N/m}$ and the polytropic constant for CO_2 $\gamma_g = 1.304$.

At the far-field, a time-varying pressure BC in which $p_\infty = p_0 - p_{ac}\sin(2\pi f_{ac}t)$ is set to begin with a drop in pressure which causes the bubble to expand first. The bubble dynamics in the original experiments[88] were found to be accurately predicted by the RPE using $p_{ac} = p_0$ and $T_{ac} = 0.24\,$ms ($f_{ac} \approx 4167\,$Hz), where T_{ac} is the time period of the pressure signal. It was previously shown in Sec. II B that the EoS for each phase is defined as $\rho_i = p\psi_i$. This definition requires the absolute pressure p to always be positive so as to return a positive density ρ to the solver.[69,70] The pressure-based nature of `compressibleInterFoam` thus prevents it from being usable for values of $p_{ac} \geqslant p_0$, since this will result in negative or zero values of pressure p and consequently, negative or zero values of density ρ, leading to solution divergence. For this reason, a smaller but

comparable forcing amplitude of $p_{ac} = 0.95\,p_0$ has been applied here, while the frequency f_{ac} is unchanged. Zero-gradient BCs are applied for α and $\mathbf{U}$ at the far-field. At the axis of rotational symmetry, the symmetry-plane BC is enforced for each solution field variable. Forced bubble oscillation described by a similar set of boundary and initial conditions will from hereon be referred to as the Acoustically-Driven Growth and Collapse (ADGC) cases.

2. *Meshing strategy*

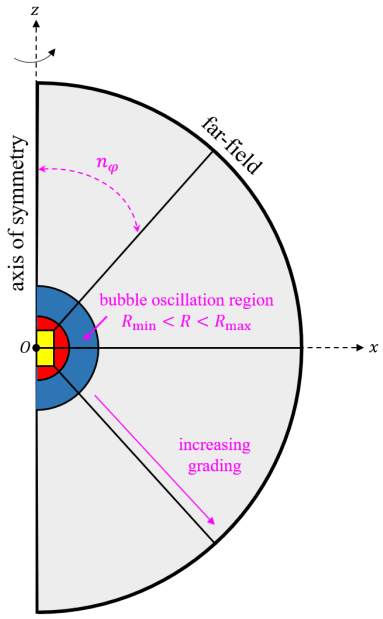

FIG. 1. Schematic diagram (not to scale) describing the O-grid mesh construction. Colour-coding is used to distinguish blocks belonging to different regions sharing similar mesh alignment, grading factors and cell aspect ratio.

An O-grid topology (see Fig. 1) is used since it maintains the known spherical symmetry of the problem to a higher degree than a standard Cartesian mesh.[56,57,62] The size of the computational domain is $D \approx 16R_{\max}$, with the maximum radius $R_{\max}$ predicted from the RPE solution for $p_{ac} = 0.95p_0$. On the basis that the bubble is centered at the origin O in Fig. 1, the O-grid mesh construction is assembled around a central core region meshed with uniform Cartesian grids (yellow block in Fig. 1). The cell alignment changes from Cartesian to radial in the 'transition' region (red blocks in Fig. 1) and extends radially outwards to the far-field in the surrounding blocks. The bubble pulsation is restricted within the blue blocks of Fig. 1, where the mesh cells have an aspect ratio (AR) of unity for a high quality mesh along the interface. The size of the bubble pulsation region is informed from the RPE solution to cover the oscillation cycle of the interface between $R_{\min} < R < R_{\max}$. Thus, when the bubble reaches its minimum size $R_{\min}$, the interface does not cross the transition region in the mesh. By restricting the bubble pulsation to be contained within the radially aligned region of the mesh, the stability of the interface is maintained. Outside the bubble pulsation region, in the gray shaded blocks of Fig. 1, the mesh is also radial but the grading factor is increased gradually in the direction of the far-field boundary (AR $\neq$ 1). The independent variable n_φ in Fig. 1 defines the number of cells per 45° sector. Grid convergence studies for $n_\varphi = 45, 90, 135$ were conducted, with $n_\varphi = 90$ providing the optimum balance between numerical accuracy and computational cost with a deviation of $< 0.68\,\%$ from the actual collapse time predicted by the RPE solution. The finest resolution ($n_\varphi = 135$) only improves this to $\approx 0.64\,\%$ with

the largest deviation of $\approx 0.8\,\%$ observed on the coarse grid ($n_\varphi = 45$).

3. *Radius history and bubble shape*

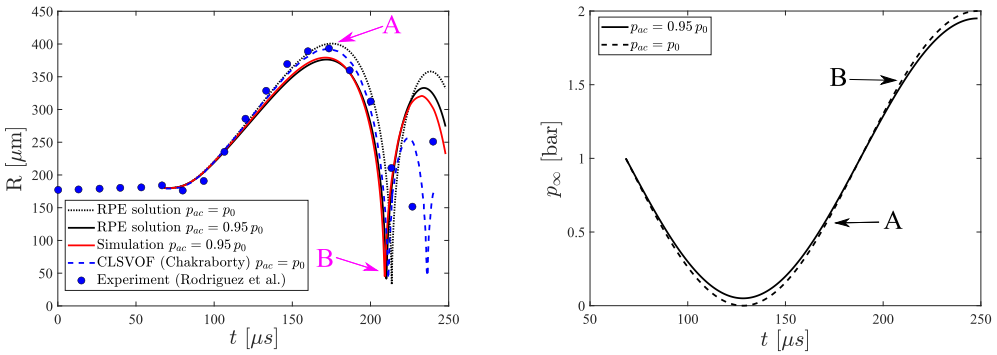

(a) (b)

FIG. 2. (a) Comparison of the equivalent radius history of the present VOF simulation result with numerical data[83] and experimental data[88]. The equivalent RPE solutions using the different p_{ac} are included for reference. (b) The far-field pressure p_∞.

Fig. 2(a) compares the results obtained using the present VOF model with the experimental data[88] and the CLSVOF simulation[83]. Note that the numerical and analytical results have been shifted by $68\,\mu$s to match the time at which the expansion wave reaches the bubble in the experiments. Initially, the bubble is in static equilibrium with the surrounding liquid. As the pressure at the far-field drops below atmospheric (see Fig. 2(b)), the bubble begins to grow until it reaches its maximum volume expansion, indicated by point 'A' in Fig. 2(a). The pressure at the far-field increases continually and as it progresses into the compressional half-cycle, the bubble collapses rapidly (point 'B' in Fig. 2(a)) and rebounds to a fraction of the size it attained during the first cycle. In Fig. 2(a), while the time at which the bubble collapses to minimum volume and minimum bubble radius computed by the present model ($t_{\mathrm{min,VOF}} = 209.1\,\mu$s and $R_{\mathrm{min,VOF}} = 45.2\,\mu$m) compare reasonably well with the RPE prediction ($t_{\mathrm{min,RPE}} = 210.2\,\mu$s and $R_{\mathrm{min,RPE}} = 41.6\,\mu$m), there is a substantial offset from the experimental measurements ($t_{\mathrm{min,EXP}} = 226.8\,\mu$s and $R_{\mathrm{min,EXP}} = 151.6\,\mu$m). Particularly, in the experiments, the size of the bubble at collapse is much larger and the collapse time is much delayed compared to those computed in the VOF simulations. A similar offset exists between the collapse time predicted by the CLSVOF method of Chakraborty[83] ($t_{\mathrm{min,LS}} = 211.4\,\mu$s and $R_{\mathrm{min,LS}} = 41.9\,\mu$m) and the experiments. This discrepancy in minimum size and collapse time can be attributed to the fact that in the VOF simulation the bubble remains intact, while in the experiments the bubble breaks into a cloud of bubbles upon collapse. Beyond this point (indicated by 'B' in Fig. 2(a)), the RPE is no longer suitable to describe the bubble dynamics as the assumption of a single isolated bubble no longer holds[88] and the value $R_{\mathrm{min,EXP}}$ therefore represents the equivalent-sphere radius for the cloud. Any deductions on bubble shape from these experiments would therefore be unreasonable.

Interestingly, a difference is observed between the bubble shape computed by the CLSVOF method[83] and the VOF method of the present study. In the CLSVOF simulations of Chakraborty[83], the bubble translates downwards during collapse and assumes a toroidal shape revealing the onset of jet formation. However, jetting has not been observed in the results obtained using the present VOF model. Jet formation is expected in situations where a source of asymmetry exists in the flow-field; for instance a nearby rigid wall that destroys the radial symmetry of the flow-field surrounding the bubble, giving rise to a pressure gradient across the bubble which drives the jet. Since in the present model, mathematically there is no such asymmetry to disrupt the surrounding pressure field, the bubble remains perfectly spherical throughout the entire acoustic cycle, as shown in Fig. 3. Note

that R_0 and R_{reb} denote the initial and rebound radius attained by the bubble in the after-bounce, respectively.

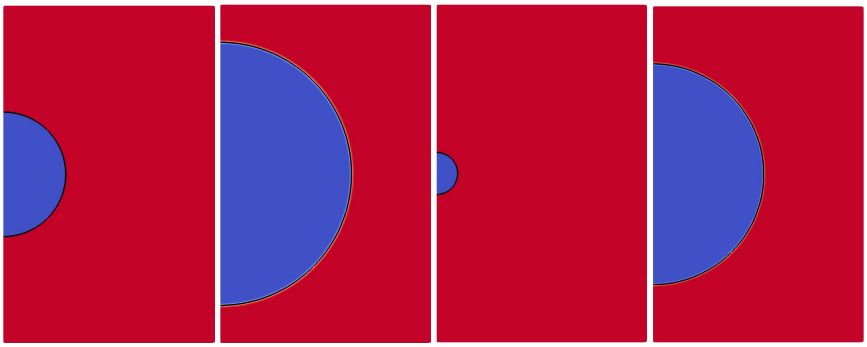

FIG. 3. Key simulation snapshots showing the bubble shape at $R = R_0, R_{\max}, R_{\min}, R_{\text{reb}}$ (from left to right).

B. Nonspherical bubble oscillation: Unforced collapse in a narrow gap

1. *Simulation setup*

Next we present a qualitative comparison of the computed bubble shape with the experimental high-speed images of Gonzalez-Avila *et al.*[27] for a laser-induced bubble confined between two opposing walls. At the walls, the BCs are no-slip for the velocity, zero-gradient for the volume fraction α and `fixedFluxPressure` for the pressure p. The latter adjusts the pressure gradient such that the flux on the boundary is that specified by the velocity BC. Note that for this validation case only, the far-field pressure BC is set to constant atmospheric pressure ($p_\infty = p_0$, $p(t) = 0$) in line with the experiments, with zero-gradient conditions for the volume fraction and velocity. In contrast with Sec. III A 1 where the initial conditions were defined by Eq. (10), here the initial conditions are a high-pressure of $p_B = 1300\,\text{bar}$ in a $50\,\mu\text{m}$ bubble in a stagnant liquid, initialised $250\mu\text{m}$ below the upper wall. Unforced bubble dynamics described using a similar combination of boundary and initial conditions will from hereon be referred to as Rayleigh Growth and Collapse (RGC) dynamics. In this section, the aim is specifically to reproduce Fig. 3 in Gonzalez-Avila *et al.*[27].

Recursive refinement is used to mesh the axisymmetric computational domain, having dimensions of 5 mm in the radial direction and $750\,\mu\text{m}$ in the vertical direction. The technique involves first meshing the domain using a coarse grid consisting of 100 cells and 15 cells in the radial and vertical directions respectively; followed by the application of five levels of refinement. The coarse grid consisting of only 1500 cells increases to ~ 0.36 million cells on the refined grid (where the original coarse uniform grid size of $50\,\mu\text{m}$ is reduced to $\sim 1.5625\,\mu\text{m}$ in the bubble region), comparable to that quoted in Ref. 27.

2. *Comparison with high-speed images*

The results are presented in Fig. 4 as alternate rows, where the first row shows the time-sequence of grayscale high-speed images obtained from the experiments of Gonzalez-Avila *et al.*[27] and the next row shows the computed bubble shape extracted as the thresholds of $\alpha_g \geq 0.5$, using the VOF methodology of Sec. II. In each simulation snapshot, the confining walls are located at the top and bottom extents of each frame and the numbers in the top left corner represent the time in microseconds (μs). Note that the time interval between the frames in the time sequence is not constant, especially during the jetting phase (third set of images in Fig. 4). Each computational

frame shows a section-plane through the rotational geometry reflected about the axis of symmetry to obtain a 2D representation.

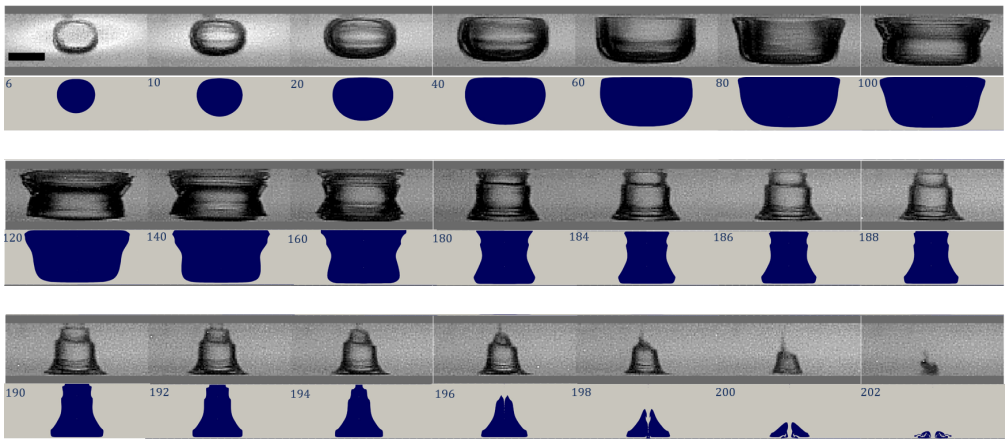

FIG. 4. Alternate rows show the grayscale frames of high-speed images from the experiments of Gonzalez-Avila *et al.*[27] and the newly-computed bubble shape in dark blue thresholds of $\alpha_g \geq 0.5$ for the transferred-jet.[68] In the first frame the scale bar length is $500\,\mu$m. Reproduced with permission from J. Fluid Mech 884, A23 (2019). Copyright 2019 Cambridge University Press.

Detailed descriptions of the flow-field evolution for this case can already be found in Ref. 27 and are beyond the scope of this validation study. Instead, only a brief overview is provided here. The time sequence in Fig. 4 starts at $t = 6\,\mu$s, with the bubble is initialised closer to the upper wall. The high internal gas pressure drives the growth, with the upper wall restricting expansion of the bubble in that direction. In the final stages of the expansion stage, the interface in the vicinity of the nearest wall becomes flatter as it moves closer to the wall but never touches it. Due to the confining walls, the growth takes place mostly along the radial direction reaching maximum volume expansion in the last frame of the first row at $t \approx 100\,\mu$s. In the second set of images ($120 < t\,(\mu\text{s}) < 188$), the collapse stage is shown where the high curvature regions near the centre of the bubble begin to shrink rapidly, forming an 'hourglass' shape (see $t = 160\,\mu$s). Beyond this point, the bubble begins to shrink rapidly from the top, forming a jet that impacts onto the opposite lower wall at $t \approx 198\,\mu$s and spreads along the boundary in the subsequent frames. This type of jetting behaviour was referred to as the 'transferred jet' in a later publication by the same research group,[68] since the jet impacts onto the wall opposite to that where the bubble was initialised. A detailed discussion on the mechanisms of jet formation in confinement will be presented in Sec. IV E.

The agreement in the time-sequence of Fig. 4 is excellent, with the bubble reaching its maximum size at $t \approx 100\,\mu$s and the jet impacting the lower boundary at $t \approx 198\,\mu$s as also found by Gonzalez-Avila *et al.*[27]. The maximum extension of the bubble in the radial direction R_x at $t = 100\,\mu$s in the simulations is $\approx 745\,\mu$m which is comparable to the $748\,\mu$m quoted in Ref. 27. Given that Gonzalez-Avila *et al.*[27] have also compared their experimental results with OpenFOAM calculations, such good agreement is expected albeit not guaranteed.

The model verification and validation studies presented in this section help emphasise the different physics modelled in the simulations. In the ADGC case of Sec. III A, the simulations start with a bubble at its equilibrium size, with an internal pressure comparable to the static pressure ($p_B/p_0 \sim 1$) in the liquid such that the bubble has zero acceleration initially. Instead, the dynamics of growth and collapse is controlled by the fluctuations in the far-field pressure, and the violent collapse is a consequence of the increasing far-field acoustic pressure at the boundary. In contrast, in the RGC case of Sec. III B, the maximum acceleration of the interface occurs at $t = 0$ due to the pressure of the gas inside the bubble being (often orders of magnitude) higher than the static pressure in the liquid ($p_B/p_0 \sim 1000$). This is generally the approach used when simulating laser-induced (or similar energy-deposit[89]) bubbles in experiments, where the pressure at the far-field is the static atmospheric pressure ($p_\infty = p_0$). While the verification study in Sec. III A demonstrates the numerical accuracy of the solution algorithm, the validation study in the present subsection pro-

vides confidence in the model's ability to capture real-world physics, particularly the dynamics of highly-confined gas bubbles.

IV. RESULTS: CONFINED ACOUSTICALLY-DRIVEN CAVITATION

A. Simulation setup

The computational setup in Fig. 5(a) shows the bubble initialised between two opposite rigid walls. The BCs are the same as those in Sec. III B except for an oscillatory pressure field $p_\infty = p_0 - p_{ac}\sin(2\pi f_{ac}t)$ imposed at the gap outlet. Since the acoustically-driven growth and collapse (ADGC) of a bubble are being modelled, the initial gas pressure for a bubble of size $R_0 = R_n$ is that specified by Eq. (10) such that the bubble is initially in equilibrium with the surrounding liquid prior to excitation by the externally applied pressure field p_∞.

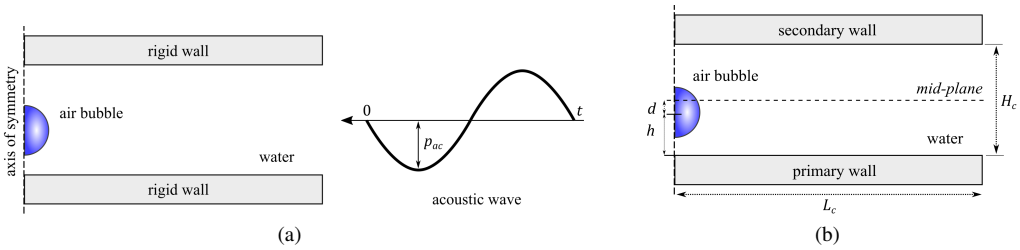

FIG. 5. (a) Sketch illustrating computational setup and BCs. Bubble is located between two rigid walls with a strong low-frequency oscillatory pressure imposed at the gap outlet. (b) Schematic illustrating geometric dimensions used to define nondimensional parameters for subsequent analysis.

Recursive mesh refinement is used to concentrate the refinement in the bubble region. The initial coarse grid consists of 100 cells in the radial direction ($L_c = 1\,\text{mm}$) with the number of cells in the axial direction modified according to the relevant gap height $H_c = [130\,\mu\text{m}, 330\,\mu\text{m}]$ to achieve a uniform coarse grid with a size of $10\,\mu\text{m}$ initially. Subsequently, the coarse grid is refined recursively five times to obtain the finest resolution of $\Delta x \approx 0.3125\,\mu\text{m}$ in the bubble region. Further refinement of the near-wall region down to a first-cell height of $\Delta y \approx 10\,\text{nm}$ is introduced to resolve the flow in the boundary layer. The cell count varies with the gap height but is on the order of ~ 0.5 million cells. As an indication, the execution time of an axisymmetric simulation with 0.47 million cells computed on 112 cores with 4571MB per core is around 10 hours.

B. Modified Rayleigh-Plesset Model

A modified RPE that resembles the standard (unmodified) RPE in Eq. (9) can be derived. It includes some additional terms to account for the geometrical confinement on the left-hand side of the equation although it neglects viscous effects. For a bubble oscillating in between two parallel disks, a modified RPE can be written as follows:[90]

$$R\ddot{R}\left[1+\frac{R}{H}\left(\ln\left[\frac{L_c}{H}\right]-1\right)\right]+\frac{3}{2}\dot{R}^2\left[1+\left(\frac{4R}{3H}\right)\left(\ln\left[\frac{L_c}{H}\right]-1\right)\right]=\frac{1}{\rho_l}\left[p_{g,n}\left(\frac{R_n}{R}\right)^{3\gamma_g}-\frac{2\sigma}{R}-p_\infty\right], \tag{11}$$

where $H = H_c/2$ denotes *half* the gap height H_c, with the other parameters having a similar meaning as in the standard RPE of Eq. (9). The sketch in Fig. 6 illustrates the configuration described by the modified RPE. The form of Eq. (11) extends itself well to the axisymmetric configuration in the simulation since rotation about the axis of symmetry will result in a 3D cylindrical equivalent similar to that in Fig. 6. The circular disk configuration will from hereon be referred to as the

(narrow) 'gap', for brevity. The modified RPE shares similar assumptions with the standard RPE, additionally assuming that the bubble is located at the centre of the gap. Regardless of the degree of confinement, it is still assumed that the bubble remains spherical throughout its entire oscillation cycle.

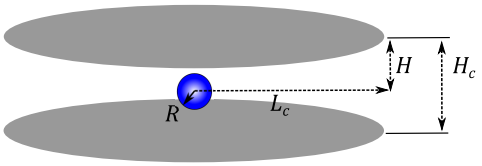

FIG. 6. Sketch illustrating the disk configuration described by the modified RPE of Leighton[90]. The bubble of size R is located at the centre and is assumed to remain spherical.

The modified RPE is used to inform the simulation setup, particularly the acoustic forcing parameters p_{ac} and f_{ac} required to instigate a transient response. For $L_c = 1\text{mm}$ and $120\,\mu\text{m} < H_c < 330\,\mu\text{m}$ considered here, $p_{ac} = 95\,\text{kPa}$ and $f_{ac} = 20\,\text{kHz}$ give an inertial response. Details on the choice of the acoustic forcing frequency are found in the Appendix B. The initial radius R_0, or the bubble radius in absence of the acoustic forcing, is chosen to represent a small transient cavitation bubble that is larger than the Blake critical radius (the lower threshold) but smaller than the Minnaert resonant radius (the upper threshold) as detailed in Appendix C. For the given acoustic signal, a bubble with an initial radius $R_0 = 50\,\mu\text{m}$ undergoes violent collapse. Fig. 7 compares the solution to the modified RPE (Eq. (11)) for $H_c = 150\,\mu\text{m}$ with the unmodified (standard) RPE (Eq. (9)) for similar acoustic forcing parameters. The graph reveals the gap confinement decreases the amplitude of oscillation of the bubble for similar acoustic forcing, and decreases the frequency of oscillation. The confinement therefore significantly alters the dynamics of bubble oscillation compared to the unconfined case.

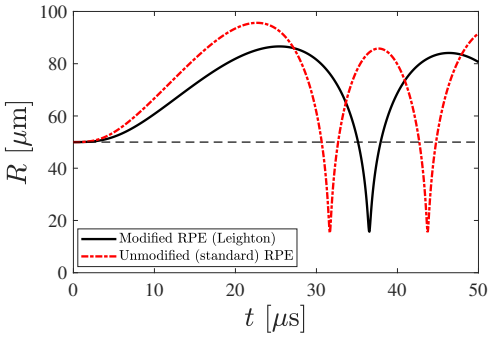

FIG. 7. Solutions of modified RPE[90] and unmodified (standard) RPE for similar acoustic forcing, here $p_{ac} = 95\,\text{kPa}$ and $f_{ac} = 20\,\text{kHz}$.

C. Collapse regimes

Both the gap height H_c and the distance h between the initialisation position of the bubble centre and the primary (lower) wall have been varied (see Fig. 5(b)), revealing three different collapse regimes. An overview of the computed bubble shape in each regime over the entire duration of the acoustic cycle is shown in Fig. 8, showing the expansion to maximum volume and subsequent collapse.

Nondimensional parameters are introduced to characterize the collapse regimes in later sections

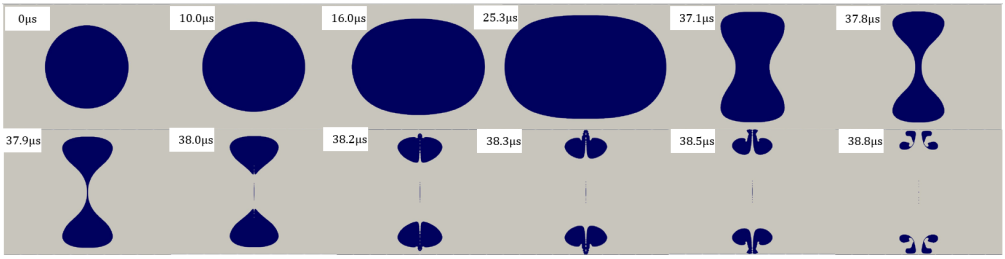

(a)

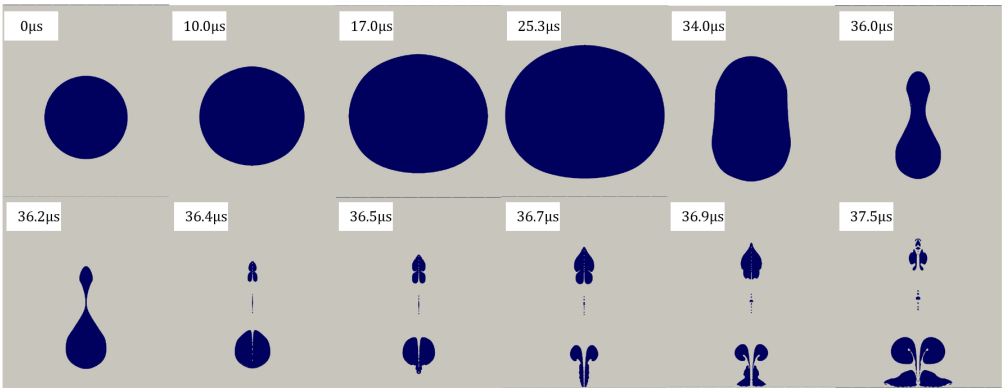

(b)

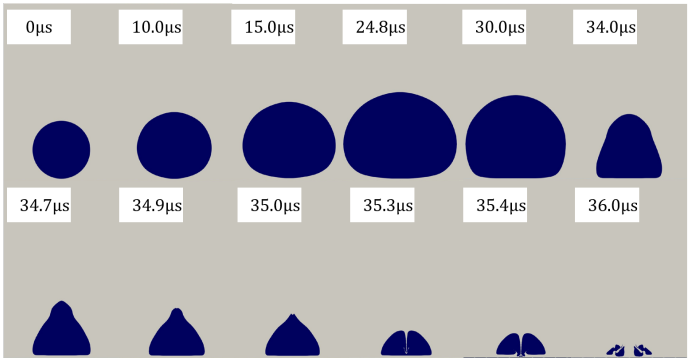

(c)

FIG. 8. Overview of collapse regimes revealed for the ADGC of a gas bubble in a narrow gap. (a) Symmetric splitting with dual-jet formation for $h = 75\,\mu$m and $H_c = 150\,\mu$m ($\eta = 1.57$ and $\delta = 0$), (b) asymmetric splitting with dual-jet formation for $h = 95\,\mu$m and $H_c = 230\,\mu$m ($\eta = 2.40$ and $\delta = 0.21$), and (c) collapse onto nearest wall with a directed jet for $h = 55\,\mu$m and $H_c = 310\,\mu$m ($\eta = 3.24$ and $\delta = 1.05$). The top and bottom extents of each frame coincide with walls while only a fraction of the radial direction is shown.

as follows. The first is the *dimensionless gap height*, η, defined as:

$$\eta = \frac{H_c}{R_{\max}}, \tag{12}$$

and the second is the *normalized off-centre distance*, δ, defined as:

$$\delta = \frac{H - h}{R_{\max}} = \frac{H_c/2 - h}{R_{\max}}, \tag{13}$$

with the primary (lower) wall taken as the datum reference for the measurement of the height h of the bubble centre above the wall. A value of $\delta = 0$ therefore corresponds to the limiting case when

the bubble is located at the centre of the gap ($h = H_c/2$). Setting the numerator $(H_c/2 - h) = d$, the definition of δ is analogous to the stand-off distance $\gamma_1 = h/R_{\max}$ for a single rigid wall but measured relative to the gap mid-plane $\delta = d/R_{\max}$. In fact, the two can be shown to be related through simple geometrical parameters as $\delta = H_c/2R_{\max} - h/R_{\max} = \eta/2 - \gamma_1$. The normalized off-centre distance δ is therefore regarded as an indicator of the position of bubble initialisation relative to the wall closest to the bubble, here taken as the primary (lower) wall (see Fig. 5(b)). For the given initial radius $R_0 = 50\,\mu$m, the smallest h simulated is $55\,\mu$m to ensure an initially detached bubble and an initial liquid layer of at least $5\,\mu$m thickness wetting the nearby walls. Using this information, the smallest stand-off distance of the bubble from the primary wall considered is $\gamma_1 \approx 0.58$. Similarly, γ_2 is the stand-off distance measured with respect to the secondary (upper) wall. The maximum spherical equivalent bubble radius in the unconfined counterpart, $R_{\max}$, is taken as the characteristic length of the problem to define nondimensional parameters.[49,55,76] The unconfined maximum radius is chosen since this is independent of the influence of nearby boundaries. Here $R_{\max} \approx 96\,\mu$m as visible from the standard (unmodified) RPE solution in Fig. 7.

1. *Regime 1 – Symmetric splitting with dual-jet formation*

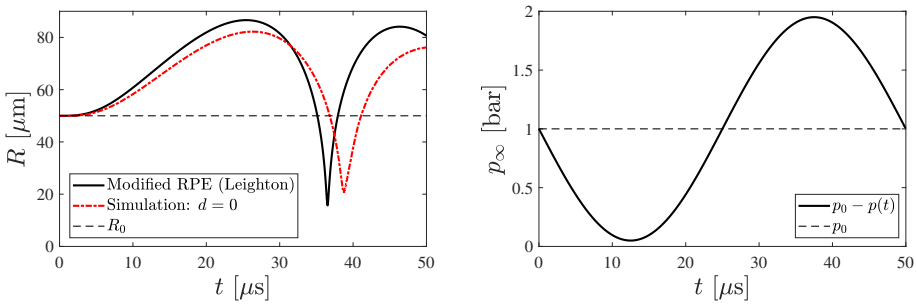

FIG. 9. (a) Comparison of modified RPE solution and equivalent simulation for limiting case $\delta = 0$ and $\eta = 1.57$ ($H_c = 150\,\mu$m and $h = 75\,\mu$m). (b) One-cycle of the low-frequency acoustic forcing signal with $p_{ac} = 0.95\,p_0$ and $f_{ac} = 20$kHz. In both graphs, the black dashed lines show the (a) bubble size and (b) far-field pressure values in absence of acoustic excitation.

Naturally, the simulation results of the limiting case when the bubble is at the centre of the gap ($d = 0$) are presented first to enable comparison with the modified RPE solution of Leighton introduced in Sec. IV B. Fig. 9(a) compares the bubble size evolution predicted by the modified RPE solution and computed bubble radius for $H_c = 150\,\mu$m in response to the acoustic forcing signal shown in Fig. 9(b). The slight deviation between the analytical and simulation results in Fig. 9(a) can be attributed to a number of factors, including the disregard of viscous forces in the modified RPE. The viscous forces in the computational model dampen the collapse relative to that predicted the modified RPE, and the bubble rebounds to a smaller size. We speculate, but have not proven, that computations using the CLSVOF method of Chakraborty[83] (which is based on physics models similar to those of this work) would reveal a similar deviation from the modified RPE. This is a plausible conjecture considering both VOF & CLSVOF techniques have shown excellent agreement in Fig. 2(a). The simulations also reveal that the spherical assumption is violated, with the bubble shape becoming highly non-spherical at maximum expansion followed by subsequent splitting and jetting events (see Fig. 8(a)). While Eq. (11) predicts the collapse times with reasonable accuracy, it does not provide any information on the bubble shape or velocities of jets that are expected to form during transient collapse of a confined bubble.

Detailed pressure and velocity field evolutions for the collapse stage are shown in Fig. 10. In these 2D representations, the left-half of each frame plots the pressure field while the right-half plots the velocity. Superimposed glyphs (arrows) in the right half of each frame indicate only the

direction (without magnitude) of the flow. Note that the colour bar ranges vary significantly between each frame. In Fig. 10, the initially spherical bubble begins to grow under the action of the imposed

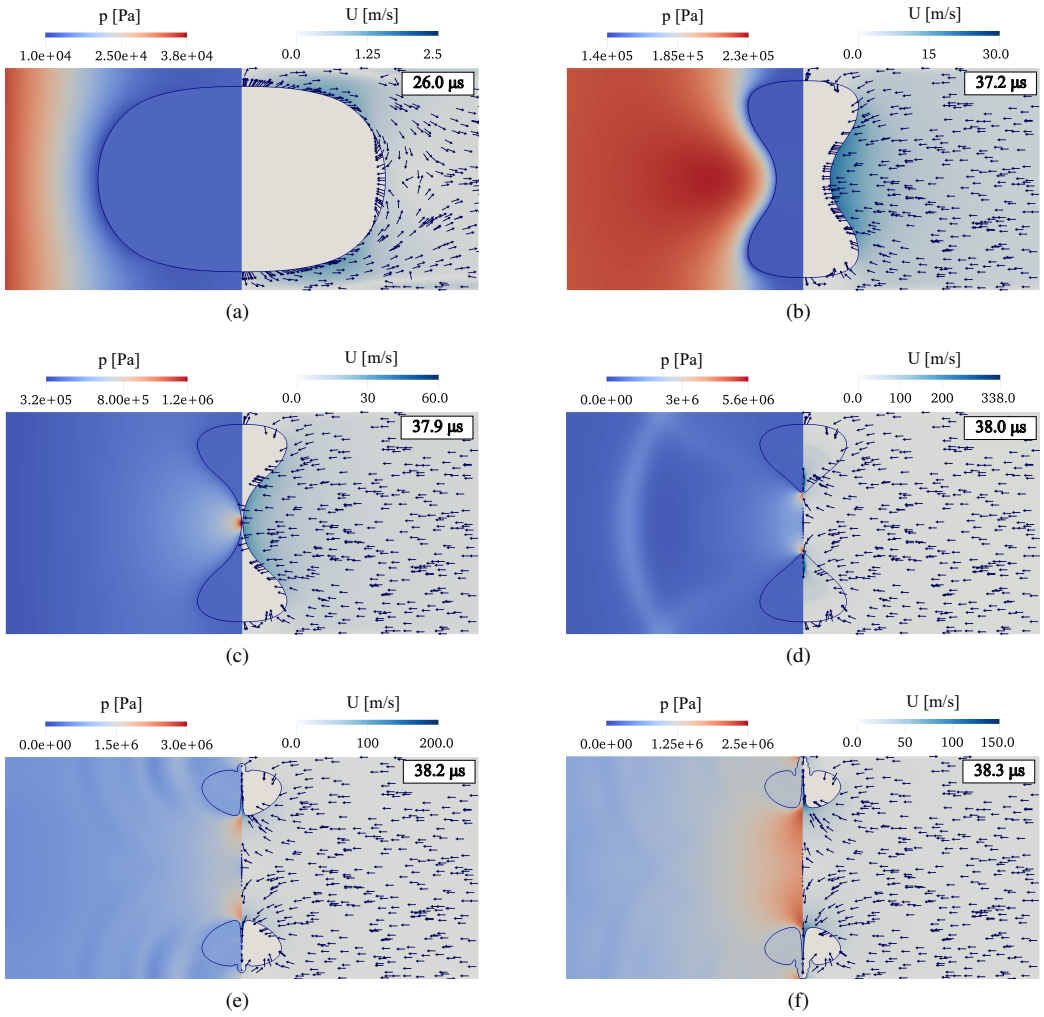

FIG. 10. Pressure and velocity field evolution starting from maximum volume expansion of the bubble, showing splitting and jet formation for limiting case $d = 0$ for $H_c = 150\,\mu$m (Regime 1). In (a) $26\,\mu$s, (b) $37.2\,\mu$s, (c) $37.9\,\mu$s, (d) $38.0\,\mu$s, (e) $38.2\,\mu$s and (f) $38.3\,\mu$s, the arrows indicate the direction of the flow-field.

far-field pressure, reaching its maximum volume at $t \approx 26\,\mu$s with a spherical equivalent radius of $\approx 82\,\mu$m. At this point, the sphericity of the bubble is entirely lost, as expansion in the axial direction is prohibited by the proximity of the nearby walls that deflect flow in the opposite direction and towards the bubble centre, which for $\delta = 0$ also coincides with the mid-plane of the gap. In the radial (lateral) direction, the expansion of the bubble is counteracted by the increase in pressure at the boundary. The reversal in direction of the glyphs in the right half of the frame at $t = 26\,\mu$s indicates the onset of the collapse stage. As the driving pressure on the boundary increases, the liquid rushes in towards the centre of the bubble accelerating its shrinkage. When the deflected flow from the walls meets the inflow from the pressure boundary, an annular flow-focussing mechanism is formed that causes the bubble to neck and form an 'hourglass' shape at $t = 37.2\,\mu$s. With the continued increase in the driving pressure, the necking proceeds rapidly reaching a maximum curvature at $t = 37.9\,\mu$s. The thin neck breaks shortly after at $t = 38\,\mu$s, separating the original bubble into two daughter bubbles. Since the case has vertical symmetry, i.e. $\delta = 0$, the bubbles formed are equal in size. The splitting event is accompanied by the emission of a spherical wave (seen propagating

outwards at $t = 38\,\mu$s) as a result of the high-pressure concentration at the neck of the bubble.

Following the splitting, the previously annular inflow is converted into two opposing axial jets each directed away from the mid-plane of the gap towards the nearest rigid wall, as visible at $t = 38.2\,\mu$s. Each of these jets propagates through the respective daughter bubble pushing the opposite bubble interface along with them as indicated by the protrusions in the same frame. Further pressure wave emission is observable at $t = 38.2\,\mu$s as a result of the jet impact onto the opposite bubble interface. The complex interference pattern in Fig. 10(e) is a result of 'shock-boundary' interactions. The first pressure wave is emitted during the splitting event at $t = 38\,\mu$s (Fig. 10(d)) where some (weak) pressure waves due to reflections at the boundary can already be observed. This is followed by the emission of two subsequent pressure waves associated with dual-jet impact. These are also reflected at the confining wall boundaries and overlap with earlier emissions, resulting in the complex interference pattern visible at $t = 38.2\,\mu$s (Fig. 10(e)). As a result, the number of pressure waves visible at $t = 38.2\,\mu$s exceeds the total of three pressure waves one would expect (splitting & dual-jet impact). During this time, the emitted pressure waves also interact with the still increasing far-field pressure p_∞ (see Fig. 9(b)). Some small satellite bubbles observed at the axis of symmetry ($38\,\mu$s onwards) are considered residues of the neck closure. After the axial jets pierce the respective bubbles, they proceed to impact and spread along the boundary at $t = 38.3\,\mu$s. Given the symmetry of the problem about the mid-plane of the gap for $\delta = 0$, we term this as the 'symmetric-splitting with dual-jet formation', or 'Regime 1', and we refer to it as such in the remainder of this study.

2. *Regime 2 – Asymmetric splitting with dual-jet formation*

By altering the bubble inception position, a second collapse regime is revealed for non-zero off-centre distance ($\delta \neq 0$). The computed bubble shape evolution is shown in Fig. 8(b) for $\eta = 2.40$ and $\delta = 0.21$. Splitting of the original bubble is still observed, however, since the vertical symmetry has been destroyed, the two daughter bubbles formed are unequal in size and their jetting profiles differ significantly. Following jet impact and collapse, the lower larger bubble is sheared along the wall surface during its rebound stage, while the upper smaller bubble is still far from the secondary wall (see $t = 37.5\,\mu$s).

The corresponding detailed pressure and velocity field evolutions for Regime 2 are shown in Fig. 11. The non-spherical shape of the bubble at $t = 25.3\,\mu$s at maximum expansion is more rounded given the wider gap ($\eta = 2.40$), but expansion in the axial direction is still limited by the presence of the walls. In this second regime, an annular flow-focussing mechanism is also observed when the deflected flow from the walls meets the inflow from the imposed acoustic forcing. As this inflow accelerates, the necking proceeds rapidly (see $t = 34\,\mu$s and $t = 36\,\mu$s) forming a thin neck ($t = 36.2\,\mu$s) that splits shortly after ($t = 36.5\,\mu$s). However, the bubble centre no longer coincides with the geometrical centre of the gap so the two daughter bubbles are of different size; the largest one being that closest to the confining boundary. A high-pressure region visible at $t = 36.5\,\mu$s is responsible for the involution and jetting of the lower bubble. This larger bubble proceeds to impact the primary wall at $t = 37.2\,\mu$s with a very pronounced jet. A complex interference between pressure (shock) waves emanating from the splitting and jet impact events can be seen at $t = 36.5\,\mu$s as they also interact with the confining boundaries.

3. *Regime 3 – Collapse onto nearest wall with a directed-jet*

Further widening of the gap and for a sufficiently large off-centre distance δ, the bubble is only minimally (if at all) affected by the secondary wall. Instead, it behaves as if it were located near a single rigid wall,[50,64,89,91] revealing a third collapse regime (see Fig. 8(c)). The corresponding detailed pressure and velocity field evolutions for Regime 3 are shown in Fig. 12. The initially spherical bubble reaches its maximum volume at $t = 24.9\,\mu$s. The distal part of the bubble remains mostly spherical, while the proximal part is flattened out due to the presence of the nearby wall. Upon reversal of pressure driving at the boundary, the bottom interface shrinks rapidly, while the

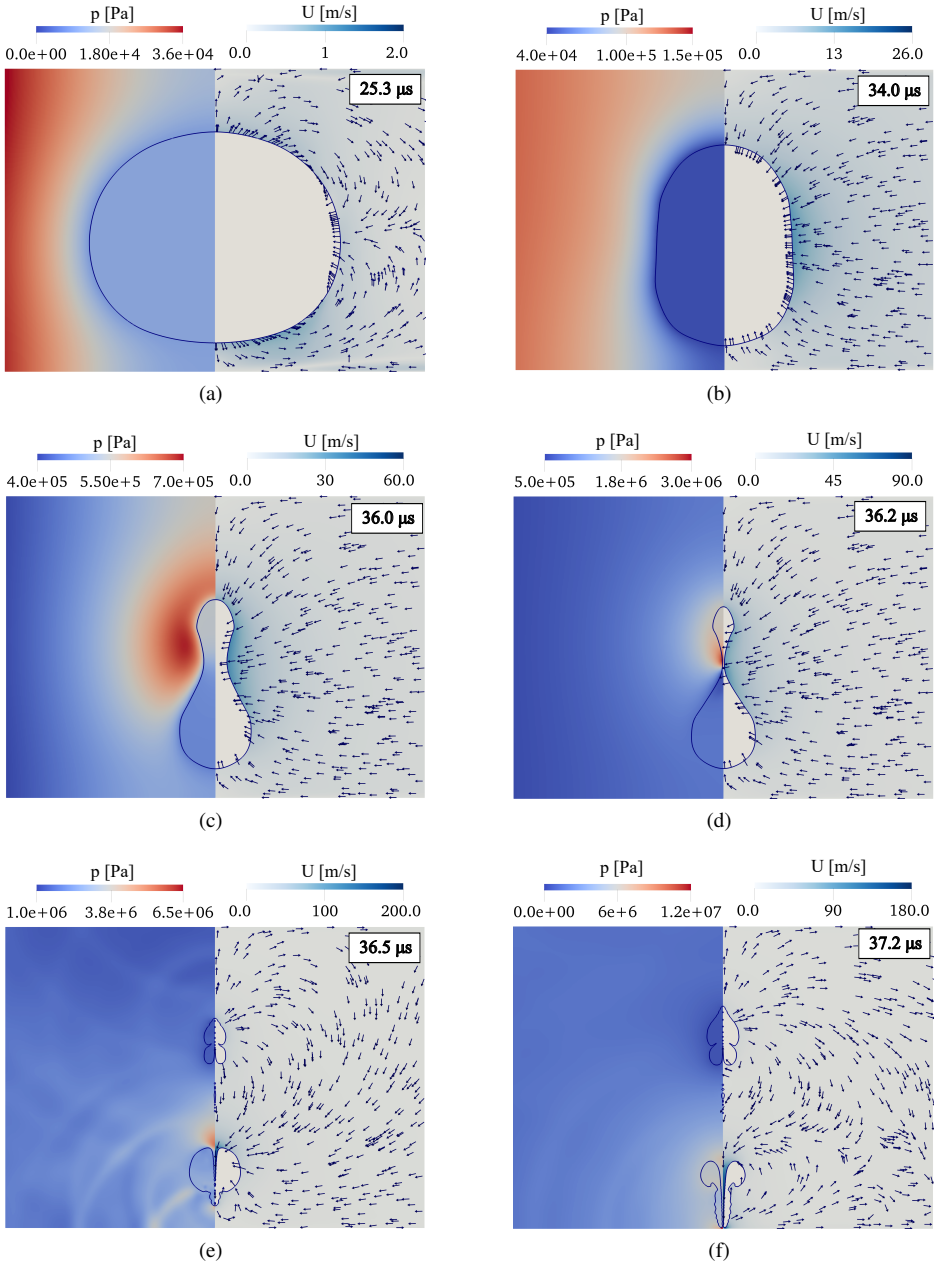

FIG. 11. Pressure and velocity field evolution starting from maximum volume expansion of the bubble, showing splitting and jet formation for $H_c = 230\,\mu$m and $h = 95\,\mu$m (Regime 2). In (a) 25.3 μs, (b) 34 μs, (c) 36 μs, (d) 36.2 μs, (e) 36.5 μs and (f) 37.2 μs, the arrows indicate the direction of the flow-field.

distal part remains relatively spherical ($t = 34\,\mu$s). As the shrinkage progresses, the curvature of the distal part of the bubble increases (see frame $t = 34.7\,\mu$s). The high-pressure region above the distal half of the bubble forms an involution at $t = 35\,\mu$s, revealing the onset of jet formation. The jet becomes more visible at $t = 35.3\,\mu$s as it propagates downwards through the bubble. The jet proceeds to pierce the bubble and impact onto the lower wall at $t = 35.4\,\mu$s.

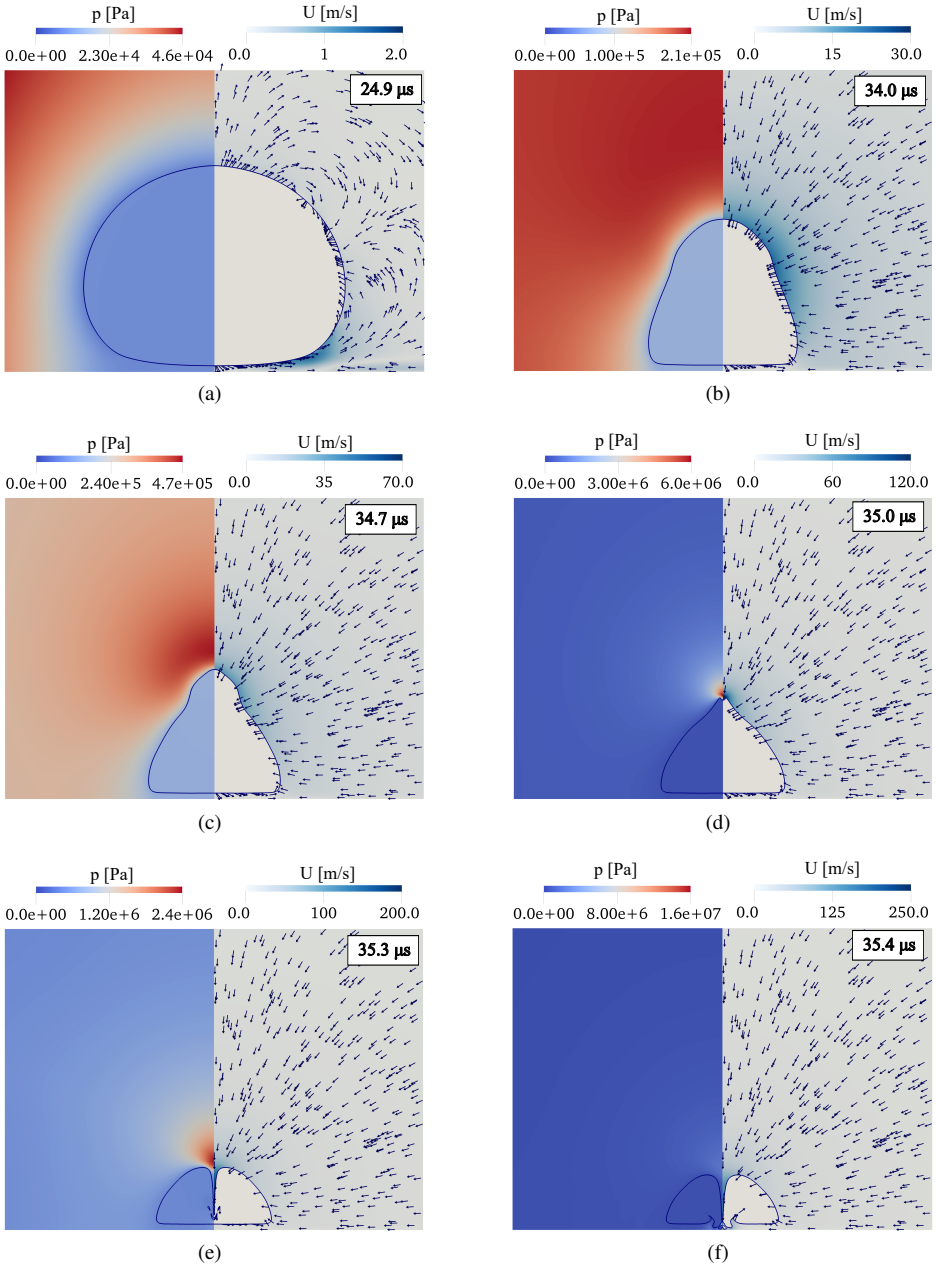

FIG. 12. Pressure and velocity field evolution starting from maximum volume expansion of the bubble, showing splitting and jet formation for $H_c = 310\,\mu$m and $h = 55\,\mu$m (Regime 3). In (a) 24.9 μs, (b) 34 μs, (c) 34.7, μs, (d) 35 μs, (e) 35.3 μs and (f) 35.4 μs, the arrows indicate the direction of the flow-field.

D. Regime mapping

A systematic study of various bubble inception positions h and gap heights H_c has been performed to map the various regimes for a given combination of dimensionless gap height, η, and off-centre distance, δ. The resulting 'regime map' in which δ is plotted against η is shown in Fig. 13. The symmetric cases are obviously segregated along the horizontal line $\delta = 0$ and correspond to the limiting case described by the modified RPE (Eq. (11)). For η values in the range $1.25 < \eta \lesssim 2.20$, a shift in the bubble initialisation position (increasing δ) will not eliminate splitting and both

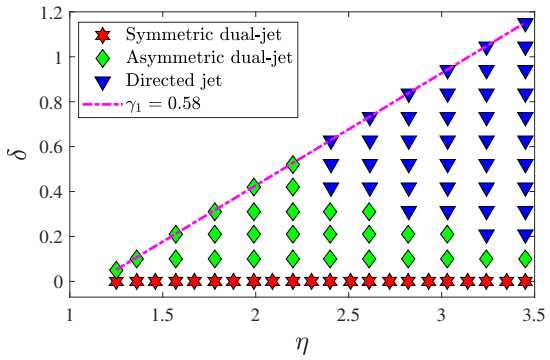

FIG. 13. Regime map identifying the relevant collapse regime for given set of nondimensional parameters η and δ for an ADGC of a bubble in a narrow gap. The dash-dot line corresponds to the closest stand-off distance considered in this study $\gamma_1 = 0.58$.

walls are exposed to (strong) shear flow due to the jet impact. However, as the gap becomes wider $2.40 \lesssim \eta \lesssim 3.03$, there appears to be a threshold of δ beyond which the splitting can be suppressed and a single jet is formed directed towards the nearest boundary, in this case, the primary lower wall. As the gap width increases even further $\eta \gtrsim 3.24$, the directed jet regime becomes even more prominent. Still, for small δ values $\delta \lesssim 0.1$, the bubble is close to the mid-plane of the gap and therefore splitting will always be observed as the limiting case of Regime 1 (when $\delta = 0$) is approached. For each η value considered, the largest δ corresponds to the closest stand-off distance of the bubble, $\gamma_1 \approx 0.58$ considered in this study.

Previous experimental and numerical studies for oscillations in a narrow gap have observed a 'transferred-jet' regime for $\eta < 1.8$, in which a single jet is formed that impacts onto the distant wall.[27,39,68] An example of this transferred-jet regime has been simulated as part of the validation study in Sec. III B for an RGC-type bubble with a pressure-ratio of $p_B/p_0 \approx 1300$[27] at the interface. For the transferred-jet to form, the bubble must be initialised very close to one wall in a gap of height H_c comparable to $R_{\max}$. This transferred-jet regime, has not been observed in the present configuration. Instead, for η values in the same range, the collapse dynamics are solely described by the splitting regimes of Sec. IV C 1 and IV C 2.

We hypothesise that the transferred-jet regime is only observed for RGC-type bubbles, where the high-pressure ratio at the interface (typically $p_B/p_0 \approx 1000$) provides the initial strong acceleration required for the bubble to expand rapidly and fill the width of the gap, leaving an extremely thin liquid-film ($\approx 5\,\mu$m) separating the bubble from the nearest wall. As the proximal interface of the bubble shrinks, a kink is formed (high-curvature) in the boundary layer that acts as a catalyst for the transferred-jet formation (see frames at $t = 194\,\mu$s in Fig. 4 for a visual example). The interested reader is referred to Zeng, Gonzalez-Avila, and Ohl[68] for full details on the origins of a transferred-jet. In the present configuration for an ADGC bubble oscillating in a narrow gap, the initial pressure-ratio at the interface is $p_B/p_0 \approx 1$, and therefore the bubble lacks the initial strong acceleration that is crucial for the formation of the transferred-jet in narrow gaps $\eta < 1.8$. Furthermore, for the closest stand-off distance $\gamma_1 = 0.58$ indicated by the dash-dotted line in the regime map, the initial ($t = 0$) liquid-film thickness between the proximal bubble interface and the primary wall is $5\,\mu$m (not shown), comparable to that reported for the transferred-jet.[68] The absence of this jetting regime is therefore attributed to the different physics being simulated in the ADGC bubble of the present configuration.

E. Intensification of micro-jet velocity

Since the initial and acoustic forcing conditions are unchanged, the velocity (including direction) of any jet(s) formed in the narrow gap configuration is only a function of the geometrical

confinement as described by η and δ. As demonstrated in Sec. IV C the collapse dynamics varies significantly over the parameter space, making a consistent definition of 'jet impact' in each regime a challenging task. Besides the strength of the jet, the width of the jet also varies considerably with off-centre distance δ. The jet is much thinner than the size of the bubble in the radial direction and highly unstable, such that it decays into droplets along the axial direction as it pierces the bubble. This makes the identification of an appropriate time to measure the 'jet impact' velocity complicated. To ensure a rigorous definition that is common to all three regimes, we take the maximum (over time and space) liquid velocity component perpendicular to the rigid wall boundaries, U_y. By sampling positive and negative values of this velocity component, it is possible to distinguish between an upward and downward jet velocity, respectively. This is of particular relevance in situations where splitting is observed (i.e. Regimes 1 and 2). For all regimes, this maximum value coincides with the velocity of the jet tip at the onset of axial jet formation. As it propagates through the bubble, the jet will be slowed down by the presence of the gas, and therefore the velocities provided here are to be regarded as an upper bound. Despite this, the sampling technique still provides an indication of when in the parameter space the maximum jet impact velocities are to be expected.

First we seek to understand how the confinement affects the jet velocity by studying the variation of jet velocity for a fixed δ value over the range of η values considered in this study ($1.25 < \eta < 3.45$). Conveniently, the dynamic behaviour described by Regime 1 for $\delta = 0$ lends itself well to this purpose. The graph in Fig. 14(a) plots the maximum axial jet velocity $U_{y,\text{jet}}$ in the liquid against η. Given the symmetry of the problem for the Regime 1 cases, the upward and downward jet velocities plotted in Fig. 14(a) are equal. For highly confined bubbles, $\eta \lesssim 1.99$, the jet velocities are ~ 300 m/s. As the gap becomes wider $\eta \gtrsim 3$, the maximum jet velocity decreases to the order of 100 m/s. This is because in wider gaps the strength of the annular flow-focussing is reduced. By conservation of momentum, the resulting axial flow velocity is also less. In the region $1.99 \lesssim \eta \lesssim 2.82$, an increase in the jet velocity is observed, reaching around ~ 400 m/s which can be regarded as the optimum combination of acoustic forcing and confinement that maximizes jet velocity.

Secondly, we seek to understand how the jet velocity changes with position of bubble inception. Here, the reverse approach is taken, namely fixing η and varying δ. Given the various regimes observed for differing η, the jet velocity is studied for three representative η values, correspond-

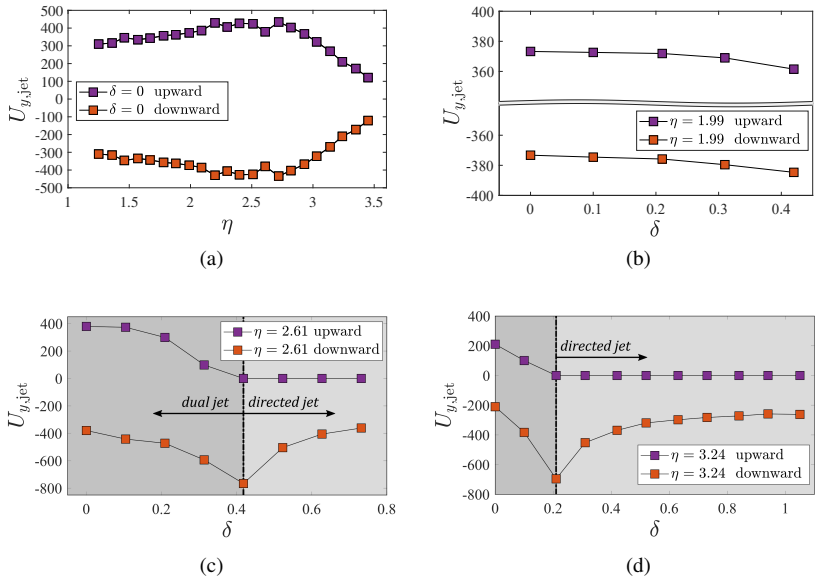

FIG. 14. Jet velocity variation $U_{y,\text{jet}}$ (m/s) for the various regimes. (a) Symmetric cases (Regime 1, $\delta = 0$), (b) Asymmetric cases (Regime 2, $\eta = 1.99$), (c) Transition from asymmetric to directed jet regimes (Regime 2 to 3, $\eta = 2.61$), and (d) Directed jet regime (Regime 3, $\eta = 3.24$).

ing to: an entirely asymmetric jet regime; a directed-jet regime observed in wider gaps; and an η value for which a transition from asymmetric to directed jet regime is observed (Figs. 14(b) - 14(d)). The asymmetric regime (Regime 2) for $\eta = 1.99$ is considered first in Fig. 14(b). At $\delta = 0$, equal and opposing jets exist due to the vertical symmetry of Regime 1 (see Fig. 14(a)). For $\delta > 0$, the splitting results in two opposing jet velocities, but now unequal in magnitude because the symmetry about the mid-plane is destroyed. As δ increases, an increase in the downward jet velocity (pertaining to the lower bubble, closer to the confining boundaries) is observed. Contrastingly, the maximum upward jet velocity (pertaining to the upper bubble) occurs for the symmetric case $\delta = 0$ and decreases monotonically with increasing off-centre distance δ. The variation in the magnitude is not as significant as for the symmetric cases, with the largest upward and downward jet velocities being comparable in magnitude, $U_{y,\text{jet}} = 373\,\text{m/s}$ for $\delta = 0$ and $U_{y,\text{jet}} = -384\,\text{m/s}$ for $\delta = 0.42$, respectively. Note that the equivalent upward velocity is $U_{y,\text{jet}} = 362\,\text{m/s}$ for $\delta = 0.42$.

Next, the maximum jet velocity for the transition regime is studied. In Fig. 14(c) the gray shaded regions are used to distinguish between δ values for which either a dual-jet or a directed jet is formed. For $\delta < 0.42$ (corresponding to Regime 2 as per the regime map of Fig. 13), the variation in maximum jet velocity is similar to that in Fig. 14(b), with the two jets acting in opposing directions but unequal in magnitude. The upward velocity is correspondingly seen to drop sharply to zero for $\delta > 0.42$ since for the directed jet regime no splitting occurs, resulting in a single jet that points downwards. The variation in downward jet velocity here is much more drastic than for $\eta = 1.99$, with the largest downward velocity peaking at $\approx -800\,\text{m/s}$ at $\delta = 0.42$. Beyond $\delta \geq 0.42$, the downward velocity decreases monotonically with increasing δ, but still remains considerably higher than the equivalent velocity observed for a similar collapse dynamics near a single rigid wall.

For the directed jet regime (see Fig. 14(d)), the first two δ values indicate a non-zero upward velocity for the symmetric and asymmetric cases described therein respectively. For such small values of δ, a degree of splitting will always be observed due to the symmetry of the problem. Beyond $\delta > 0.21$, splitting does not occur; the absence of an upper daughter bubble implies a zero jet velocity in the upward direction. The characteristic peak downward velocity observed previously in Fig. 14(c) of $\sim -800\,\text{m/s}$ is also observed here, albeit for a different δ value, and decreases monotonically with increasing δ. However, the decreased confinement in this wider gap ($\eta = 3.24$ compared to $\eta = 2.61$) results in a much smaller downward velocity at the maximum δ.

Overall, an intensification of the jet velocity on the order of several hundred meters per second is observed in this configuration. This is considerably higher than the jet velocities reported for collapse near a single rigid wall, typically around $100\,\text{m/s}$ [53,64,89,91] with wall shear stresses on the order of 100 kPa.[64] An exception occurs for very close stand-off distances $\gamma_1 \lesssim 0.1$ for which Lechner *et al.*[55,76] report velocities on the order of 1000 m/s for viscosity-/curvature- induced jets. Such small stand-off distances are not considered in the present study. Lechner *et al.*[55] attributed this order of magnitude increase in jet velocity to a different mechanism of jet formation that had not previously been observed. In contrast, for the stand-off distances considered in this study, the enhancement in jet velocity is purely a consequence of the interplay between the deflected flow from the walls and the inflow from the imposed acoustic forcing. Interestingly, Lechner *et al.* have identified the modelling of the expansion stage (not just the collapse stage) and the inclusion of viscous effects are responsible for these incredibly fast jets. Considering the above, the modelling of viscous effects and the growth stage in numerical models of bubble dynamics can no longer be overlooked.

F. Wall shear stress footprint

The no-slip condition at the walls gives rise to a velocity gradient perpendicular to the boundary and results in a shear stress on the surface.[92] Therefore, the enhanced jet velocities reported in Sec. IV E will inevitably lead to stronger bubble-induced forces on the nearby boundaries responsible for cleaning (or eroding) the surface. The wall shear stress (WSS) on a planar wall, τ , is defined as:

$$\tau = \mu \left. \frac{\mathrm{d}U_x}{\mathrm{d}y} \right|_{y=0}, \tag{14}$$

where μ is the viscosity of the fluid, U_x is the velocity in the radial direction and y is the perpendicular distance from the wall, such that $y = 0$ lies on the boundary.[93,94] Experimental measurement of wall shear stress from acoustic cavitation bubbles is difficult, since the formation of acoustic bubbles is harder to control compared to the more repeatable laser-induced bubbles. In computational simulations, the WSS can be approximated by:

$$\tau \approx \mu_l \left. \frac{U_x(y)}{y} \right|_{y \leq \varepsilon}, \tag{15}$$

where ε is the constant shear region in the boundary layer and μ_l is the viscosity of the liquid.[27,64,95] The WSS is measured in the near-wall regions where the velocity gradient is relatively constant.[64] Here, it is sampled at a distance of $y = 10\,\text{nm}$ from each wall. This sampling location is located within the thin liquid-film that separates the bubble from the nearby boundary and therefore the viscosity of the liquid can be used to calculate the WSS. While the height of this liquid-film decreases with decreasing stand-off distance γ_1, the film persists even for the largest δ (i.e. the smallest stand-off distance) for which $h_f \sim 5\,\mu\text{m}$. In the event that the bubble comes into contact with the wall(s), or interferes with the sampling location of the WSS, the mixture viscosity would need to be considered. In this section, the shear-stress variation for representative cases belonging to each regime is studied to understand the influence of acoustic forcing on the WSS.

In the following sections, the WSS footprint on boundaries is studied for representative cases from each regime. Both the instantaneous WSS distribution (during splitting and jet impact) and the spatio-temporal distribution (over one acoustic cycle) are considered. The range of shear stress magnitude on the boundaries varies considerably (orders of magnitude) over the growth and collapse cycle of a bubble, from a few kPa up to several thousand kPa. To obtain a better understanding of this complex spatio-temporal variation, we plot 'wall-shear-stress maps' depicting the shear stress evolution in the bubble region before, during and after the collapse.[64] These are contour plots in which positive and negative shear stresses are colour-coded. Given the orders of magnitude difference in shear stress, τ, the logarithm of the shear stress is plotted, such that $\log_{10}\tau = 6$ indicates a shear stress magnitude on the order of $\sim$MPa. Here, *positive* values of shear stress (indicating flow directed *away* from the axis of symmetry at $x = 0$) are coloured in purple, while *negative* values of shear stress (indicating flow directed *towards* the axis) are coloured in green. The corresponding radius-history curve is overlayed in each map to correlate the shear stress evolution with the bubble dynamics (e.g. peak shear stress occurring at minimum bubble volume).

1. Symmetric - Regime 1

The wall shear stress maps in Fig. 15 for $\eta = 1.57$ and $\delta = 0$ ($H_c = 150\,\mu\text{m}$ and $h = 75\,\mu\text{m}$) show how the maximum WSS occurs very close to the axis of symmetry ($x = 0$) at the instant of minimum volume when the jet impacts the opposite bubble interface at the end of the collapse stage. Since the symmetric regime is considered here, Figs. 15(a) and 15(b) for the primary and secondary walls, respectively, are identical ($\gamma_1 = \gamma_2 = 0.78$) . Some numerical instabilities begin to be observed in the region $t > 40\,\mu\text{s}$ during the rebound phase due to the distorted shape of the bubble following the violent collapse, and therefore the discussion on WSS here is focussed until shortly after the first collapse. The positive peak shear stress is seen to move radially outwards and decrease in magnitude (less dark shades) as the rebound phase begins. Note the maps plot only the WSS evolution in the bubble region $0 \leq x(\mu\text{m}) \leq 100$. The WSS is positive during most of the bubble expansion stage, and the direction is only reversed as the increase in far-field acoustic pressure counteracts further expansion of the bubble in the radial direction. During the collapse stage, this negative shear region progressively moves further inwards towards the axis as the continued increase in p_∞ accelerates the liquid inflow. The strongest shear flow arises when the bubble collapses to its minimum volume. The strength of this flow decreases in magnitude as it moves radially outwards. In the early rebound stages, the shear flow is directed away from the axis of symmetry as the high-speed flow from the liquid jet spreads along the boundary accelerating the flow in the radial direction. The positive shear flow persists for most of the rebound stage, with a negative shear flow opposing this outward-spreading jet flow present only further away from the axis at $x \geq 80\,\mu\text{m}$.

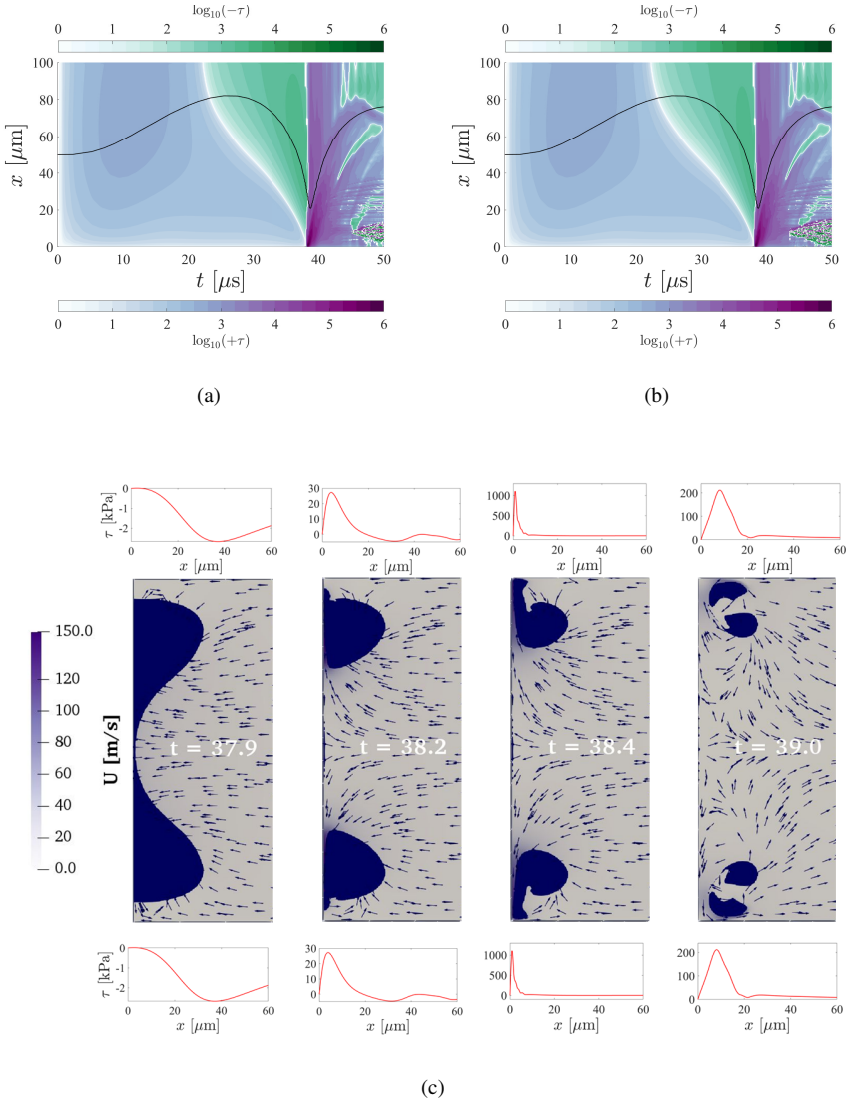

FIG. 15. Spatio-temporal wall shear stress distribution on (a) the primary wall and (b) the secondary wall. Radius-history curve is plotted as black solid line on each map to correlate shear-stress with bubble size evolution. (c) Instantaneous wall shear stress evolution for symmetric splitting with dual jet formation of Regime 1, $\eta = 1.57$ and $\delta = 0$ ($H_c = 150\,\mu$m and $h = 75\,\mu$m). Time in microseconds (μs).

Instantaneous WSS distributions on both walls are shown in Fig. 15(c) together with the corresponding snapshots of bubble shape. At $t = 37.9\,\mu$s, the pressure at the far-field boundary is still increasing, forcing the bubble to continue shrinking before splitting. After splitting, the annular inflow is converted into opposing dual-jets that pierce through the daughter bubbles (visible from the protrusions at $t = 38.2\mu$s) and proceed to accelerate the flow in the thin liquid film between the respective bubble and the walls outwards; reversing the direction of the WSS. As the jet impacts onto the boundary at $t = 38.4\,\mu$s, the shear stress reaches its maximum of $\tau \approx 1000\,$kPa on both walls. The shear stress grows from zero directly below the bubble to some maximal value in a close vicinity of the axis at $x = 0$. This peak shear stress is short-lived and decays in magnitude and spreads radially outwards with the bubble, as shown at $t = 39\,\mu$s. These key features of the shear stress footprint are well captured in the wall shear stress maps.

2. *Asymmetric - Regime 2*

Fig. 16 shows the WSS evolution for $\eta = 2.20$ and $\delta = 0.42$ ($H_c = 210\,\mu$m and $h = 65\,\mu$m). The WSS map for the primary wall shown in Fig. 16(a) is largely similar to that for Regime 1, except that the region of positive shear stress at collapse is wider and extends to $x \approx 20\,\mu$m. This is due to the lower bubble being closer to the wall at this larger δ value ($\gamma_1 \approx 0.68$). Contrastingly, the shear stress distribution on the secondary (upper) wall (see Fig. 16(b)) is considerably different to that in Fig. 15(b). Since the upper bubble is now located further away from the upper wall, the strength of the shear flow on this boundary is much weaker and no evident peak is observed. The direction of the flow alternates in time between positive and negative regions of shear flow according to whether the bubble is expanding or shrinking, but does not vary with radial distance.

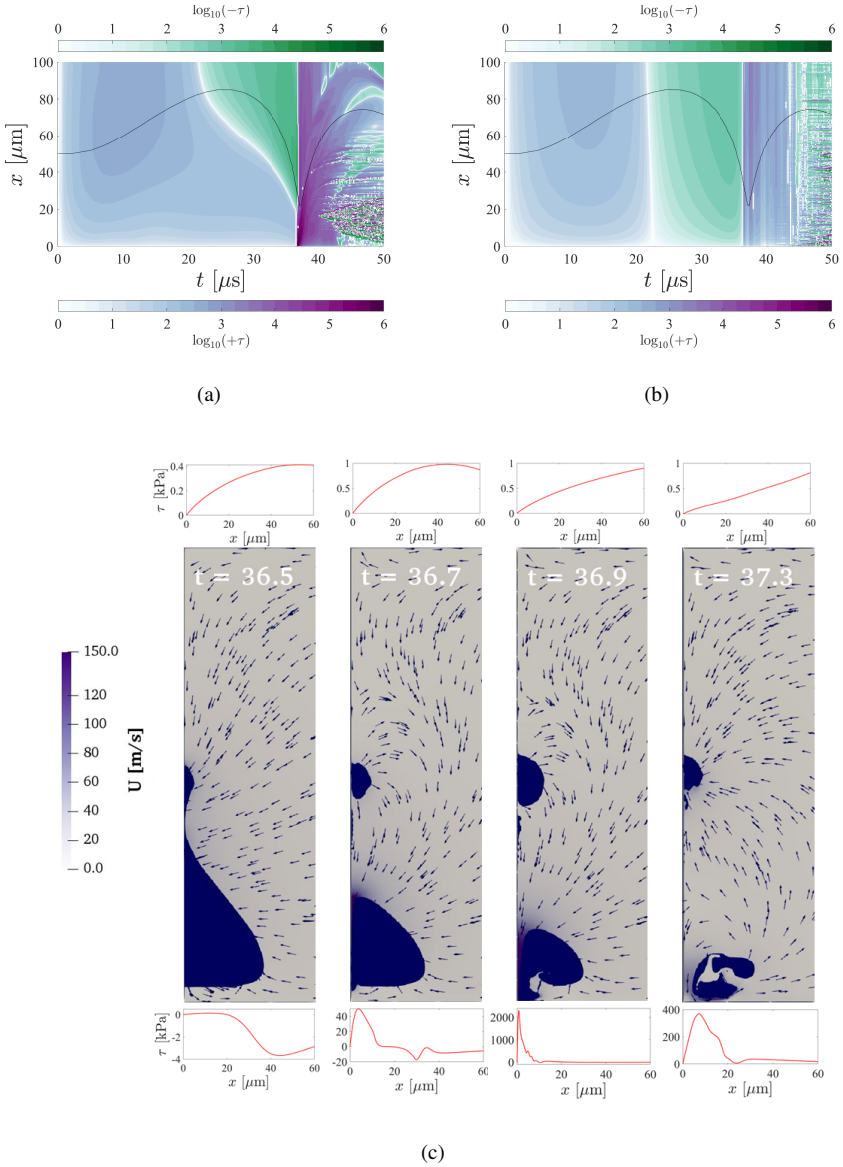

FIG. 16. Spatio-temporal wall shear stress distribution on (a) the primary wall and (b) the secondary wall. (c) Instantaneous wall shear stress evolution for asymmetric splitting with dual jet formation of Regime 2, $\eta = 2.20$ and $\delta = 0.42$ ($H_c = 210\,\mu$m and $h = 65\,\mu$m). Time in microseconds (μs).

The corresponding instantaneous shear stress distribution is shown in Fig. 16(c). In this asymmetric regime, the location of bubble collapse is shifted downwards towards the lower wall and therefore the stronger shear stresses are expected to occur on this boundary. The instantaneous distribution reveals a peak shear stress of $\approx 2000\,\mathrm{kPa}$ as the jet impacts onto the lower wall at $t = 36.9\,\mu\mathrm{s}$. An increase in shear stress on the lower wall is expected, given the bubble is initialised closer to it, but the doubling in magnitude compared to that observed in Fig. 15 is surprising. This increase in shear stress is an indication of the stronger collapse of the acoustically-driven bubble. On the upper wall, a peak shear stress is not observed. There, the WSS is only a few kilopascals in magnitude. For similar δ, moderate shear stresses on the upper wall are expected in gaps narrower than considered in Fig. 16 as the separation between the upper bubble and the secondary wall is reduced.

3. *Directed - Regime 3*

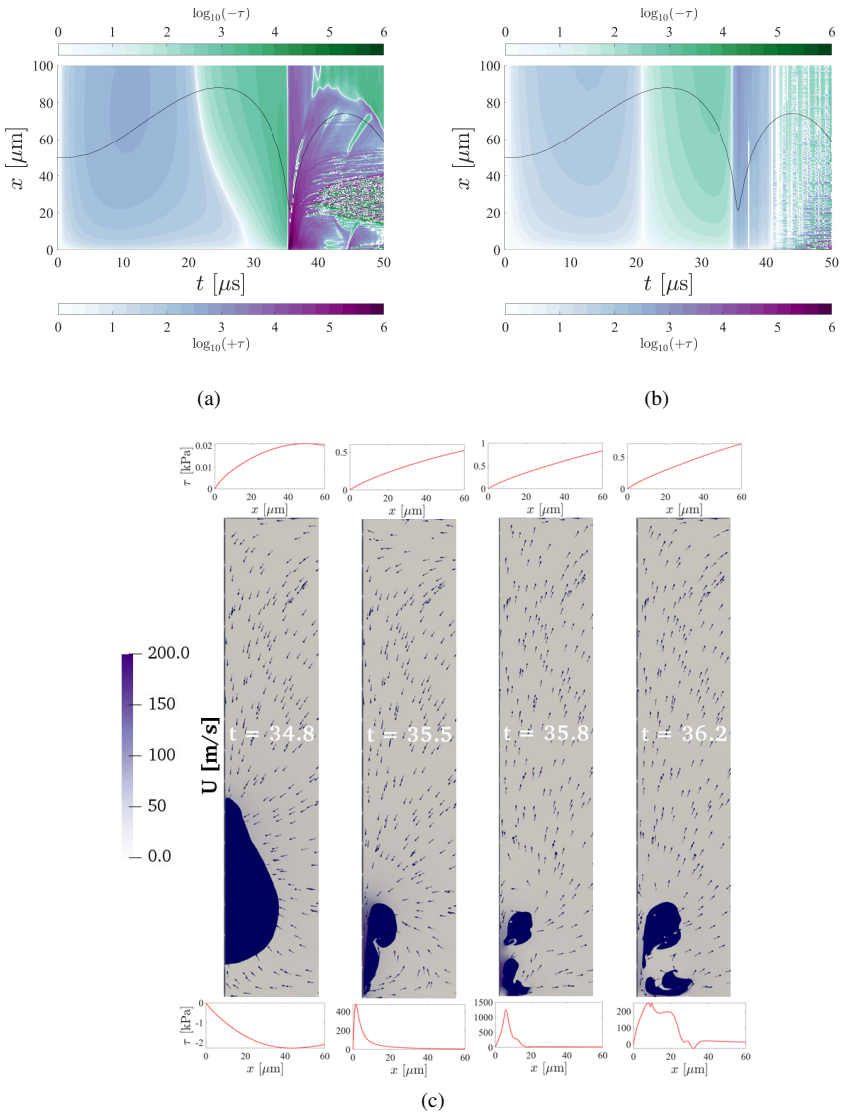

FIG. 17. Spatio-temporal wall shear stress distribution on (a) the primary wall and (b) the secondary wall. (c) Instantaneous wall shear stress evolution for collapse onto nearest wall with directed jet of Regime 3, for $\eta = 3.24$ and $\delta = 0.63$ ($H_c = 310\,\mu\mathrm{m}$ and $h = 95\,\mu\mathrm{m}$). Time in microseconds (μs).

The WSS distribution for a typical directed jet regime is shown in Fig. 17. For the case considered, $\eta = 3.24$ and $\delta = 0.63$ ($H_c = 310\,\mu$m and $h = 95\,\mu$m) the shear stress distribution on the primary wall is not too different from that shown in Fig. 16(a) for Regime 2 except that the greater separation between the primary wall and the lower bubble ($\gamma_1 \approx 1$) causes the shear flow near the axis to become negative before the collapse (see $t \approx 30\,\mu$s in Fig. 17(a)). A localised region of strong outward shear flow on the lower wall is still observed as the bubble collapses to minimum volume. As observed in the previously described regimes, this high shear stress region decreases in magnitude as it propagates outwards. On the secondary wall, no such peak stress is observed, and the direction of the shear stress alternates sharply between positive and negative regions according to the global flow direction (see Fig. 17(b)). This contrasts with the shear-stress footprint observed in Fig. 15(b) for which an obvious peak value was observed as the bubble collapses.

The corresponding instantaneous shear stress distribution is shown in Fig. 17(c). During the collapse at $t = 34.8\,\mu$s, the shear flow along the primary wall is negative reflecting the inflow during the collapse. Following jet impact, as the bubble is translated towards the lower wall, the shear stress is seen to change direction and increase in magnitude, reaching about 400 kPa at $t = 35.5\,\mu$s. A further increase in the shear flow along the bottom boundary occurs at $t = 35.8\,\mu$s with $\tau \approx 1200$ kPa. As the bubble rebounds, the amplitude of the outward shear flow decreases and fluctuations due to the highly-distorted bubble shape are observable at $t = 36.2\,\mu$s. On the secondary wall, the shear stress is orders of magnitude lower, reaching only ~ 1 kPa.

V. DISCUSSION

The shear forces along the confining boundaries have been quantified by extracting the distribution of the velocity gradient (rate of strain) close to the surface. The wall-shear-stress footprint varies with bubble-wall separation and the degree of confinement. The peak wall shear stress is observed during bubble collapse when the high-speed microjet impacts onto the wall and spreads along the surface as a thin but high-speed boundary layer.[96] Strong and localised shear stresses of up to 2 MPa are found for the acoustically-driven growth and collapse (ADGC) of a bubble considered in the present study. This peak value is twice the maximum shear stress reported for a Rayleigh Growth and Collapse (RGC) or laser-induced bubble in a similar configuration.[27] The peak stress occurs at a localised point close to the axis of rotational symmetry and is attenuated as it spreads radially outwards. Recalling that the simulations are axisymmetric, in three dimensions the maximum shear can be visualised to occur in concentric circular zones (annular rings) whose centre is directly beneath the bubble surface. Recent experimental measurements of wall shear stress and corresponding 3D simulations by Reuter *et al.*[23] for a bubble collapsing near a single rigid wall suggest that this is indeed the case.

The introduction of a secondary opposing wall has already been shown to enhance the maximum wall shear stress on boundaries for RGC bubbles, ~ 1000 kPa[27] in a narrow gap as compared to ~ 100 kPa for (single) wall-bounded collapse.[50,64] The even higher shear rates found in the present configuration (~ 2000 kPa) are attributed to the increased pressure amplitude driving the collapse, and are expected to vary with the acoustic forcing. Specifically, the transient behaviour of an acoustically-driven bubble has been considered in this study, in which a high-velocity re-entrant jet impacts onto the boundary. However, weaker shear rates (steady microstreaming) are expected for a milder forcing where the bubble oscillates stably between two parallel walls.[97]

The maximum shear stress computed compares well to some extent with the experimental observations by Maisonhaute *et al.*[92] who have found shear stresses in the range $2.5 - 5$ MPa for acoustically-driven but hemispherical bubbles. However, the measurements, made at $40 - 80$ nm from the wall, were for stable oscillations and had therefore been considered a lower bound. The maximum shear stress computed here occurs for larger off-centre distances when the detached (spherical) bubble is initialised very close to one of the walls. To better quantify this agreement for acoustic cavitation, simulations involving hemispherical bubbles could be the subject of future work. An order of magnitude discrepancy is often found between experimental measurements of the shear stress and numerical computations.[27] One drawback of experimental measurements is that, to date, these have been limited to a single point location,[21,23,98] which is restrictive as opposed to

the complete spatial and temporal distribution available in simulations. The proposed VOF model is therefore a useful tool that complements experimental investigation and provides insight into the mechanisms underlying bubble-cleaning. Improved agreement with experimental measurements for validation purposes is of course desirable, but the rapidly fluctuating strong gradients generated in the thin liquid-film between a bubble and nearby boundaries pose significant experimental challenges. Nevertheless, Reuter *et al.*[23] have achieved comparable agreement between experimental measurements and computational simulations in OpenFOAM for an RGC bubble collapsing near a single rigid wall. However, the maximum shear stress reported therein was only $\sim 5\,\mathrm{kPa}$, which still is orders of magnitude lower than that observed in the present configuration. It is also less than the $\sim 25\,\mathrm{kPa}$ computed maximal shear stress reported by Koukouvinis *et al.*[96] who simulated the growth and collapse of a laser-generated bubble. This discrepancy may be due to the fact that Reuter *et al.*[23] only compute the collapse stage of the bubble, assuming that at maximum expansion the bubble is perfectly spherical, which is rarely the case for bubbles expanding in vicinity of a wall.[48,49] Besides, the differing bubble sizes ($\sim 400\,\mu\mathrm{m}$ in Reuter *et al.*[23] compared to $\sim 700\,\mu\mathrm{m}$ in Koukouvinis *et al.*[96]), may also result in a different mechanical action on the surface.

VI. CONCLUSIONS

We have investigated the growth and collapse dynamics of an acoustically-driven bubble inside a narrow gap. The acoustic forcing introduces a further complexity in the flow-field such that the interaction of this forcing with the deflected flow from the walls plays a crucial role in the collapse. The presence of confinement combined with the imposed time-varying boundary pressure result in an oscillatory non-uniform pressure distribution around the bubble, causing it to assume a non-spherical shape at maximum expansion. As a result, we have found that the bubble collapses rapidly following one of three regimes: symmetric or asymmetric splitting with dual-jet formation (Regimes 1 and 2, respectively), or a directed jet onto the nearest wall (Regime 3). A regime map helps predict the direction of the resulting jet(s) for a given gap height (nondimensional η) and axial position of the bubble inside the gap (off-centre distance δ). Although a single bubble size has been considered in this study, it is expected that maintaining a similar ratio of gap height H_c to maximum volume $R_{\max}$ will reveal the same three collapse regimes for larger bubbles driven below their resonant frequency ($f_{ac} \ll f_c$ as detailed in the AppendixB). Existing studies for an unforced bubble in a narrow gap[26,29,34,38] suggest this is indeed the case. In future work, we will endeavour to investigate various combinations of initial bubble sizes and acoustic forcing frequencies.

As expected, bubbles initialised at the centre of the gap will always split and form two opposing jets of equal strength. This contrasts with the modified RPE prediction in which it is assumed that the bubble remains spherical at all times regardless of the degree of confinement. We have found that the induced micro-jet velocity decreases with decreasing vertical constraint (increasing η). Off-centering the bubble position will still result in dual-jet formation, but with unequal strengths. In wider gaps ($\eta \geq 3$), the dual-jet formation is suppressed for bubbles initialised close to one of the boundaries. Instead, under this reduced vertical constraint, the bubbles exhibit behaviour analogous to collapse near a single rigid wall. We have termed this as the directed-jet regime. We report on the absence of a transferred-jet regime previously observed for a laser-induced bubble in similar confinement, an unexpected finding of this study which highlights the different physics involved in acoustic cavitation simulation (ADGC-type simulation) compared to laser-induced bubbles (RGC-type simulation).

The imposed acoustic forcing dictates the spatio-temporal evolution of bubble-induced forces on nearby boundaries, and its inclusion in computational models of acoustic cavitation should not be overlooked. Through careful choice of the acoustic forcing and fluid properties, the desired dynamic behaviour to suit the application can be achieved. Despite the presented geometry being relatively simple, we emphasise that the findings of this work have significant implications not only in ultrasonic cleaning applications[18,27,39,92] but also in microfluidic applications for mixing, actuation and manipulation,[6,10,33,99–101] where the number of jets correlates with the number of boundaries confining the bubble.[102] Since the wall geometries are smooth, the simulations presented in this study are representative of configurations in which the length scale of the wall roughness is much

smaller than the nominal bubble size. Future work will aim to consider bubble collapse in more complex geometrical confinement such as curved boundaries[103], corners[104], patterned surfaces[105] or a second bubble[106].

ACKNOWLEDGMENTS

This research was supported by Waters Corporation UK and the Engineering and Physical Sciences Research Council (EPSRC) under grant EP/N016602/1. The authors acknowledge the use of the Scientific Computing Research Technology Platform, and associated support services at the University of Warwick UK, in the completion of this work. JM is indebted to Dr. Indrajit Chakraborty for interesting discussions on the subject and to Gonzalez-Avila, van Blokland, Zeng, and Ohl[27] for exchanges regarding the OpenFOAM solver. We thank the reviewers for their valuable comments that helped improve this article.

AUTHOR DECLARATIONS

The authors have no conflicts to disclose.

DATA AVAILABILITY

The data that support the findings of this study are openly available in the Warwick Research Archive Portal (WRAP) at the following link: http://wrap.warwick.ac.uk/158721/, Ref. 107.

Appendix A: Discretization schemes

Table II provides a summary of the typical discretization schemes that were used to obtain the results in this work. This choice of discretisation schemes is similar to that used in recent studies of bubble dynamics in OpenFOAM (see for instance Refs. 56, 57, 62, 66, 67, 69 amongst others). Note that corrections for mesh skewness and non-orthogonality are only required in situations were the mesh is not rectilinear.

TABLE II. Discretisation schemes (`fvSchemes`).

Term	Keyword	Scheme
Time derivatives	ddtSchemes	Euler
Divergence terms	divSchemes	
	$\nabla\cdot(\rho\mathbf{U}\mathbf{U})$	linearUpwindV
	$\nabla\cdot(\alpha_l\mathbf{U})$	vanLeer
	$\nabla\cdot(\mathbf{U}_r\alpha_l\alpha_g)$	interfaceCompression
Gradient terms	gradSchemes	linear skewCorrected linear
Laplacian terms	laplacianSchemes	linear corrected
Interpolation	interpolationSchemes	linear
Surface-normal gradients	snGradSchemes	corrected

Appendix B: Identifying the acoustic forcing frequency

Since the transient response is sought, the acoustic forcing frequency f_{ac} must be lower than the natural frequency of oscillation. The natural frequency:

$$f_n = f_{\mathrm{RPE}} = \frac{1}{2\pi}\sqrt{\frac{3\gamma_g p_0 + 2(3\gamma_g - 1)\sigma/R_n}{\rho_l R_n^2}}, \tag{B1}$$

can be derived from Eq. (9) but is strictly valid for bulk bubbles (i.e. in an unconfined volume of liquid). Here, a quantification of the reduction in the resonant frequency in confinement is desirable. A modified natural frequency of oscillation can be derived by linearising Eq. (11) by assuming small radial perturbations ξ, such that $R(t) = R_n + \xi(t)$ where $\dot{R} = \dot{\xi}$ and $\ddot{R} = \ddot{\xi}$. Substituting for $\xi, \dot{\xi}$ and $\ddot{\xi}$ in Eq. (11), multiplying by $(R_n + \xi)$ throughout and neglecting higher-order terms gives:

$$R_n^2\ddot{\xi}\left[1 + \frac{(R_n+\xi)}{H}\left(\ln\left[\frac{L_c}{H}\right] - 1\right)\right] = \frac{1}{\rho_l}\left[p_{g,n}(R_n+\xi)\left(\frac{R_n+\xi}{R_n}\right)^{-3\gamma_g} - p_\infty(R_n+\xi) - 2\sigma\right]. \tag{B2}$$

The RHS can be further simplified with the help of the negative binomial expansion:

$$\frac{1}{\rho_l}\left[p_{g,n}(R_n+\xi)\left(1 - 3\gamma_g\left(\frac{\xi}{R_n}\right)\right) - p_\infty(R_n+\xi) - 2\sigma\right].$$

Rearranging:

$$\ddot{\xi} + \frac{3\gamma_g p_{g,n} - 2\sigma/R_n}{\rho_l R_n^2\left[1 + (R_n/H)\left(\ln[L_c/H] - 1\right)\right]}\xi = \frac{-p(t)}{\rho_l R_n\left[1 + (R_n/H)\left(\ln[L_c/H] - 1\right)\right]}. \tag{B3}$$

The resulting linearised equation resembles the classical equation for a damped oscillator $\ddot{x} + \beta\dot{x} + \omega_n^2 x = F(t)$, where x is a generic coordinate frame, β is the damping coefficient, ω_n is the natural frequency and $F(t)$ is the forcing function which here is an external pressure that varies sinusoidally in time $p(t)$.[84] Therefore, the natural frequency of a bubble confined between two plates is given by:

$$\omega_c = \sqrt{\frac{3\gamma_g p_{g,n} - 2\sigma/R_n}{\rho_l R_n^2\left[1 + (R_n/H)\left(\ln[L_c/H] - 1\right)\right]}} = 2\pi f_c, \tag{B4}$$

where ω_c (rad/s) refers to the natural frequency of oscillation in the confined disk configuration of Fig. 6. The linear resonance frequency in confinement f_c can be expressed as a function of the unconfined natural frequency f_n :

$$f_c = f_n\sqrt{\frac{1}{\left[1 + (R_n/H)\left(\ln[L_c/H] - 1\right)\right]}}. \tag{B5}$$

The normalized frequency ratio f_c/f_n can be regarded as a *geometric scaling factor* for a given bubble of size R_n.

Eqs. (B4) and (B5) are used to compute the natural frequency of oscillation for $H_c = [120\,\mu\mathrm{m}, 330\,\mu\mathrm{m}]$ as considered in the computational simulations to find that $40\,\mathrm{kHz} < f_c < 60\,\mathrm{kHz}$ (see Fig. 18(a)). As expected, the confinement reduces the frequency of oscillation and this range of f_c is lower than the unconfined natural frequency $f_{\mathrm{RPE}} \approx 65.9\,\mathrm{kHz}$ predicted by Eq. (B1). However, as the gap becomes wider f_c becomes comparable to $f_n = f_{\mathrm{RPE}}$ (see Fig. 18(b)). Given the lowest f_c is $\approx 40\,\mathrm{kHz}$, an $f_{ac} = 20\,\mathrm{kHz}$ has been chosen to guarantee a transient (inertial) response ($f_{ac} \ll f_c$).

Appendix C: The initial bubble radius

A bubble actively pulsates for a wide range of ambient radius. If the size of the bubble and the acoustic pressure amplitude are sufficiently large, the bubble will oscillate transiently (i.e. unstably) in response to the pressure fluctuations. This condition is often termed as the Blake threshold,

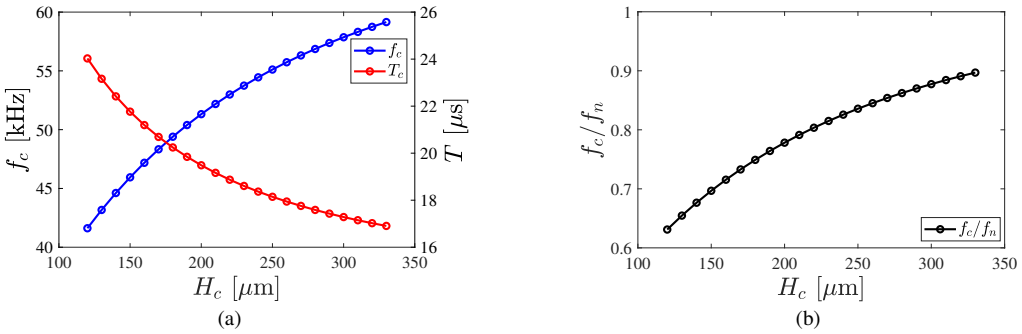

FIG. 18. (a) Confined natural frequency scaling and (b) variation of frequency ratio f_c/f_n.

defining a size above which bubbles will undergo 'explosive' initial growth in response to a decreasing fluid pressure, or tension wave, in the liquid [48,84]. The equation for Blake-threshold pressure is given as:

$$p_{\text{Blake}} = p_0 + \frac{8\sigma}{9}\left[\frac{3\sigma}{2R_{\text{Blake}}^3\left(p_0 + (2\sigma/R_{\text{Blake}})\right)}\right]^{1/2}, \tag{C1}$$

where p_{Blake} is the acoustic pressure required to generate transient cavitation [84]. Rearranging Eq. (C1) to solve for R_{Blake} gives a cubic equation:

$$2p_0R_{\text{Blake}}^3 + 4\sigma R_{\text{Blake}}^2 - \frac{3\sigma}{\left[9(p_{\text{Blake}} - p_0)/(8\sigma)\right]^2} = 0\,. \tag{C2}$$

Solution of Eq. (C2) gives three roots; however, two of these are complex conjugates such that R_{Blake} is given by the real root. For the given forcing conditions $p_{\text{Blake}} = p_{ac} = 95\,\text{kPa}$ and $f_{ac} = 20\,\text{kHz}$ with $p_0 = 100\,\text{kPa}$, $\sigma = 0.072\,\text{N/m}$, the Blake radius is $R_{\text{Blake}} = 5.2\,\mu\text{m}$.

An expression for the Minneart radius can be calculated from Eq. (B1):

$$\rho_l(2\pi f_{ac})^2R_{\text{Minnaert}}^3 - 3\gamma p_{g,n}R_{\text{Minnaert}} + 2\sigma = 0\,, \tag{C3}$$

which is also a cubic equation that can be solved for R_{Minnaert} yielding two complex conjugates and one real root. For the given acoustic forcing conditions, $p_{ac} = 95\,\text{kPa}$ and $f_{ac} = 20\,\text{kHz}$, solution of Eq. (C3) gives $R_{\text{Minnaert}} \approx 159\,\mu\text{m}$.

The upper bound of the ambient radius for an active bubble is on the same order of magnitude as the linear resonance radius R_{Minnaert}, while the lower bound coincides with the Blake threshold radius R_{Blake} [84]. The above threshold formulations are derived from Eq. (9) but are useful approximations. The initial bubble radius R_0 must be larger than the lower threshold (Blake) radius R_{Blake} and smaller than the resonant Minnaert radius R_{Minnaert} [48,49,84] such that:

$$R_{\text{Blake}} < R_0 < R_{\text{Minnaert}}\,, \tag{C4}$$

and therefore,

$$5.2\,\mu\text{m} < R_0 < 159\,\mu\text{m}. \tag{C5}$$

An initial radius of $50\,\mu\text{m}$ is chosen within the above range. This also allows for a direct comparison of the ultrasonically-driven dynamics (Sec. IV) with the validation study in Sec. III B where a similar initial radius was shown to accurately capture the bubble dynamics in the experiments.

[1] W. Lauterborn and T. Kurz, "Physics of bubble oscillations," Reports on Progress in Physics **73**, 106501 (2010).
[2] R. E. A. Arndt, "Cavitation in Fluid Machinery and Hydraulic Structures," Annual Review of Fluid Mechanics **13**, 273–326 (1981).

[3]S. Ibsen, C. E. Schutt, and S. Esener, "Microbubble-mediated ultrasound therapy: A review of its potential in cancer treatment," Drug Design, Development and Therapy **7**, 375–388 (2013).
[4]N. Vyas, K. Manmi, Q. Wang, A. J. Jadhav, M. Barigou, R. L. Sammons, S. A. Kuehne, and A. D. Walmsley, "Which Parameters Affect Biofilm Removal with Acoustic Cavitation? A Review," Ultrasound in Medicine and Biology **45**, 1044–1055 (2019).
[5]C. C. Coussios and R. A. Roy, "Applications of acoustics and cavitation to noninvasive therapy and drug delivery," Annual Review of Fluid Mechanics **40**, 395–420 (2008).
[6]D. Rabaud, P. Thibault, J. P. Raven, O. Hugon, E. Lacot, and P. Marmottant, "Manipulation of confined bubbles in a thin microchannel: Drag and acoustic Bjerknes forces," Physics of Fluids **23**, 042003 (2011).
[7]K. Kooiman, H. J. Vos, M. Versluis, and N. De Jong, "Acoustic behavior of microbubbles and implications for drug delivery," Advanced Drug Delivery Reviews **72**, 28–48 (2014).
[8]T. H. Kim and H. Y. Kim, "Disruptive bubble behaviour leading to microstructure damage in an ultrasonic field," Journal of Fluid Mechanics **750**, 355–371 (2014).
[9]G. L. Chahine, A. Kapahi, J. K. Choi, and C. T. Hsiao, "Modeling of surface cleaning by cavitation bubble dynamics and collapse," Ultrasonics Sonochemistry **29**, 528–549 (2016).
[10]P. Marmottant and S. Hilgenfeldt, "Controlled vesicle deformation and lysis by single oscillating bubbles," Nature **423**, 153–156 (2003).
[11]Q. X. Wang and K. Manmi, "Three dimensional microbubble dynamics near a wall subject to high intensity ultrasound," Physics of Fluids **26**, 032104 (2014).
[12]N. Vyas, Q. X. Wang, K. A. Manmi, R. L. Sammons, S. A. Kuehne, and A. D. Walmsley, "How does ultrasonic cavitation remove dental bacterial biofilm?" Ultrasonics Sonochemistry **67**, 105112 (2020).
[13]N. Vyas, R. L. Sammons, S. A. Kuehne, C. Johansson, V. Stenport, Q. X. Wang, and A. D. Walmsley, "The effect of standoff distance and surface roughness on biofilm disruption using cavitation," PLOS ONE **15**, 1–16 (2020).
[14]T. J. Mason, "Ultrasonic cleaning: An historical perspective," Ultrasonics Sonochemistry **29**, 519–523 (2016).
[15]S. Brems, M. Hauptmann, E. Camerotto, A. Pacco, T.-G. Kim, X. Xu, K. Wostyn, P. Mertens, and S. De Gendt, "Nanoparticle Removal with Megasonics: A Review," ECS Journal of Solid State Science and Technology **3**, N3010–N3015 (2014).
[16]B. Verhaagen and D. Fernández Rivas, "Measuring cavitation and its cleaning effect," Ultrasonics Sonochemistry **29**, 619–628 (2016).
[17]W. Kim, T. H. Kim, J. Choi, and H. Y. Kim, "Mechanism of particle removal by megasonic waves," Applied Physics Letters **94**, 1–4 (2009).
[18]C. D. Ohl, M. Arora, R. Dijkink, V. Janve, and D. Lohse, "Surface cleaning from laser-induced cavitation bubbles," Applied Physics Letters **89**, 074102 (2006).
[19]S. R. Gonzalez-Avila, X. Huang, P. A. Quinto-Su, T. Wu, and C. D. Ohl, "Motion of micrometer sized spherical particles exposed to a transient radial flow: Attraction, repulsion, and rotation," Physical Review Letters **107**, 1–4 (2011).
[20]F. Reuter and R. Mettin, "Mechanisms of single bubble cleaning," Ultrasonics Sonochemistry **29**, 550–562 (2016).
[21]R. Dijkink and C. D. Ohl, "Measurement of cavitation induced wall shear stress," Applied Physics Letters **93**, 1–4 (2008).
[22]S. R. Gonzalez-Avila, F. Denner, and C.-D. Ohl, "The acoustic pressure generated by the cavitation bubble expansion and collapse near a rigid wall," Physics of Fluids **33**, 032118 (2021).
[23]F. Reuter, H. Sagar, B. el Moctar, and R. Mettin, "Wall Shear Rates Induced by a Single Cavitation Bubble Collapse," in *Proceedings of the 10th International Symposium on Cavitation (CAV2018)* (ASME Press, 2018).
[24]J. R. Blake and D. C. Gibson, "Cavitation Bubbles Near Boundaries." Annual Review of Fluid Mechanics **19**, 99–123 (1987).
[25]O. Supponen, D. Obreschkow, M. Tinguely, P. Kobel, N. Dorsaz, and M. Farhat, "Scaling laws for jets of single cavitation bubbles," Journal of Fluid Mechanics **802**, 263–293 (2016), arXiv:1703.01088.
[26]R. Mousavi Belfeh Teymouri and G. Ahmadi, "Intensification of the Near Wall Collapsing Bubble Induced Jet Using an Opposite Secondary Wall," Journal of Fluid Science and Technology **3**, 207–218 (2008).
[27]S. R. Gonzalez-Avila, A. C. van Blokland, Q. Zeng, and C. D. Ohl, "Jetting and shear stress enhancement from cavitation bubbles collapsing in a narrow gap," Journal of Fluid Mechanics **884**, A23 (2020).
[28]L. Bai, J. Yan, Z. Zeng, and Y. Ma, "Cavitation in thin liquid layer : A review," Ultrasonics Sonochemistry **66**, 1–9 (2020).
[29]A. Shima and Y. Sato, "The behavior of a bubble between narrow parallel plates," Zeitschrift für angewandte Mathematik und Physik ZAMP **31**, 691–704 (1980).
[30]V. V. Kucherenko and V. V. Shamko, "Dynamics of electric-explosion cavities between two solid parallel walls," Journal of Applied Mechanics and Technical Physics **27**, 112–115 (1986).
[31]H. Ishida, C. Nuntadusit, H. Kimoto, T. Nakagawa, and T. Yamamoto, "Cavitation bubble behavior near solid boundaries," Fourth International Symposium on Cavitation (2001).
[32]Y. H. Chen, H. Y. Chu, and L. Lin, "Interaction and fragmentation of pulsed laser induced microbubbles in a narrow gap," Physical Review Letters **96**, 1–4 (2006).
[33]P. A. Quinto-Su, K. Y. Lim, and C.-D. Ohl, "Cavitation bubble dynamics in microfluidic gaps of variable height," Physical Review E **80**, 047301 (2009).
[34]F. I. Azam, B. Karri, S. W. Ohl, E. Klaseboer, and B. C. Khoo, "Dynamics of an oscillating bubble in a narrow gap," Physical Review E **88**, 1–7 (2013).
[35]E. W. Quah, B. Karri, S. W. Ohl, E. Klaseboer, and B. C. Khoo, "Expansion and collapse of an initially off-centered bubble within a narrow gap and the effect of a free surface," International Journal of Multiphase Flow **99**, 62–72 (2018).
[36]Z. Zhang, A. Wang, J. Wu, Y. Liu, D. Huang, Y. Qiu, and J. Li, "Spatial confinement effects of bubbles produced by laser ablation in liquids," AIP Advances **9**, 125048 (2019).
[37]A. M. Zhang, B. Y. Ni, B. Y. Song, and X. L. Yao, "Numerical simulation of bubble breakup phenomena in a narrow flow field," Applied Mathematics and Mechanics (English Edition) **31**, 449–460 (2010).

[38]B. Han, R. Zhu, Z. Guo, L. Liu, and X. W. Ni, "Control of the liquid jet formation through the symmetric and asymmetric collapse of a single bubble generated between two parallel solid plates," European Journal of Mechanics, B/Fluids **72**, 114–122 (2018).
[39]S. R. Gonzalez-Avila, E. Klaseboar, B. C. Khoo, and C.-D. Ohl, "Cavitation bubble dynamics in a liquid gap of variable height," Journal of Fluid Mechanics **682**, 241–260 (2011).
[40]B. Liu, J. Cai, and X. Huai, "Heat transfer with the growth and collapse of cavitation bubble between two parallel heated walls," International Journal of Heat and Mass Transfer **78**, 830–838 (2014).
[41]C. T. Hsiao, J. K. Choi, S. Singh, G. L. Chahine, T. A. Hay, Y. A. Ilinskii, E. A. Zabolotskaya, M. F. Hamilton, G. Sankin, F. Yuan, and P. Zhong, "Modelling single-and tandem-bubble dynamics between two parallel plates for biomedical applications," Journal of Fluid Mechanics **716**, 137–170 (2013).
[42]H. Peng, X. He, J. Zhang, and Y. Wang, "Cavitation bubble collapse between parallel rigid walls with the three-dimensional multi-relaxation time pseudopotential lattice Boltzmann method," AIP Advances **10**, 105104 (2020).
[43]M. Mohammadzadeh, F. Li, and C. D. Ohl, "Shearing flow from transient bubble oscillations in narrow gaps," Physical Review Fluids **2**, 014301 (2017).
[44]C. Chen, Y. Gu, J. Tu, X. Guo, and D. Zhang, "Microbubble oscillating in a microvessel filled with viscous fluid: A finite element modeling study," Ultrasonics **66**, 54–64 (2016).
[45]W. Wiedemair, Ž. Tuković, H. Jasak, D. Poulikakos, and V. Kurtcuoglu, "On ultrasound-induced microbubble oscillation in a capillary blood vessel and its implications for the blood – brain barrier," Physics in Medicine & Biology **57**, 1019–1045 (2012).
[46]S. Martynov, E. Kostson, N. Saffari, and E. Stride, "Forced vibrations of a bubble in a liquid-filled elastic vessel," The Journal of the Acoustical Society of America **130**, 2700–2708 (2011).
[47]A. Osterman, M. Dular, and B. Širok, "Numerical Simulation of a Near-Wall Bubble Collapse in an Ultrasonic Field," Journal of Fluid Science and Technology **4**, 210–221 (2009).
[48]B. Boyd and S. Becker, "Numerical modelling of an acoustically-driven bubble collapse near a solid boundary," Fluid Dynamics Research **50** (2018), 10.1088/1873-7005/aad58a.
[49]B. Boyd and S. Becker, "Numerical modeling of the acoustically driven growth and collapse of a cavitation bubble near a wall," Physics of Fluids **31** (2019), 10.1063/1.5084729.
[50]F. Denner, F. Evrard, and B. van Wachem, "Modeling Acoustic Cavitation Using a Pressure-Based Algorithm for Polytropic Fluids," Fluids **5**, 69 (2020).
[51]The explosive initial growth is understood to be around twice (or more) the initial size of the bubble.
[52]T. Trummler, S. H. Bryngelson, K. Schmidmayer, S. J. Schmidt, T. Colonius, and N. A. Adams, "Near-surface dynamics of a gas bubble collapsing above a crevice," Journal of Fluid Mechanics **899**, A16 (2020), arXiv:1912.07022.
[53]A. Philipp and W. Lauterborn, "Cavitation erosion by single laser- produced bubbles," Journal of Fluid Mechanics **361**, 75–116 (1998).
[54]S. Popinet and S. Zaleski, "Bubble collapse near a solid boundary: a numerical study of the influence of viscosity," Journal of Fluid Mechanics **464**, 137–163 (2002).
[55]C. Lechner, W. Lauterborn, M. Koch, and R. Mettin, "Fast, thin jets from bubbles expanding and collapsing in extreme vicinity to a solid boundary: A numerical study," Physical Review Fluids **4**, 1–7 (2019).
[56]T. Li, S. Wang, S. Li, and A. M. Zhang, "Numerical investigation of an underwater explosion bubble based on FVM and VOF," Applied Ocean Research **74**, 49–58 (2018).
[57]S. T. Miller, H. Jasak, D. A. Boger, E. G. Paterson, and A. Nedungadi, "A pressure-based, compressible, two-phase flow finite volume method for underwater explosions," Computers and Fluids **87**, 132–143 (2013).
[58]B. S. Mirjalili, S. S. Jain, and M. S. Dodd, "Interface-capturing methods for two-phase flows: An overview and recent developments," Center for Turbulence Research: Annual Research Briefs , 117–135 (2017).
[59]K. Schmidmayer, S. H. Bryngelson, and T. Colonius, "An assessment of multicomponent flow models and interface capturing schemes for spherical bubble dynamics," Journal of Computational Physics **402**, 109080 (2020).
[60]S. Popinet and S. Zaleski, "A front-tracking algorithm for accurate representation of surface tension," International Journal for Numerical Methods in Fluids **30**, 775–793 (1999).
[61]M. Sussman, A. S. Almgren, J. B. Bell, P. Colella, L. H. Howell, and M. L. Welcome, "An Adaptive Level Set Approach for Incompressible Two-Phase Flows," Journal of Computational Physics **148**, 81–124 (1999).
[62]M. Koch, C. Lechner, F. Reuter, K. Köhler, R. Mettin, and W. Lauterborn, "Numerical modeling of laser generated cavitation bubbles with the finite volume and volume of fluid method, using OpenFOAM," Computers and Fluids **126**, 71–90 (2016).
[63]C. Lechner, M. Koch, W. Lauterborn, and R. Mettin, "Pressure and tension waves from bubble collapse near a solid boundary: A numerical approach," The Journal of the Acoustical Society of America **142**, 3649–3659 (2017).
[64]Q. Zeng, S. R. Gonzalez-Avila, R. Dijkink, P. Koukovinis, M. Gavaises, and C. D. Ohl, "Wall shear stress from jetting cavitation bubbles," Journal of Fluid Mechanics **846**, 341–355 (2018).
[65]B. Han, K. Köhler, K. Jungnickel, R. Mettin, W. Lauterborn, and A. Vogel, "Dynamics of laser-induced bubble pairs," Journal of Fluid Mechanics **771**, 706–742 (2015).
[66]T. Li, A. M. Zhang, S. P. Wang, G. Q. Chen, and S. Li, "Nonlinear interaction and coalescence features of oscillating bubble pairs: Experimental and numerical study," Physics of Fluids **31**, 092108 (2019).
[67]T. Li, A. M. Zhang, S. P. Wang, S. Li, and W. T. Liu, "Bubble interactions and bursting behaviors near a free surface," Physics of Fluids **31**, 042104 (2019).
[68]Q. Zeng, S. R. Gonzalez-Avila, and C.-D. Ohl, "Splitting and jetting of cavitation bubbles in thin gaps," Journal of Fluid Mechanics **896**, A28 (2020).
[69]T. Yamamoto, S.-I. Hatanaka, and S. V. Komarov, "Fragmentation of cavitation bubble in ultrasound field under small pressure amplitude," Ultrasonics Sonochemistry **58**, 104684 (2019).

[70]T. Yamamoto and S. V. Komarov, "Liquid jet directionality and droplet behavior during emulsification of two liquids due to acoustic cavitation," Ultrasonics Sonochemistry **62**, 104874 (2019).
[71]J. U. Brackbill, D. B. Kothe, and C. Zemach, "A Continuum Method for Modeling Surface Tension," Journal of Computational Physics **100**, 335–354 (1992).
[72]H. G. Weller, "A new approach to VOF-based interface capturing methods for incompressible and compressible flow," Tech. Rep. (OpenCFD, 2008).
[73]D. A. Hoang, V. van Steijn, L. M. Portela, M. T. Kreutzer, and C. R. Kleijn, "Benchmark numerical simulations of segmented two-phase flows in microchannels using the Volume of Fluid method," Computers and Fluids **86**, 28–36 (2013).
[74]T. Yamamoto, Y. Okano, and S. Dost, "Validation of the S-CLSVOF method with the density-scaled balanced continuum surface force model in multiphase systems coupled with thermocapillary flows," International Journal for Numerical Methods in Fluids **83**, 223–244 (2017).
[75]K. J. Vachaparambil and K. E. Einarsrud, "Comparison of Surface Tension Models for the Volume of Fluid Method," Processes **7**, 542 (2019).
[76]C. Lechner, W. Lauterborn, M. Koch, and R. Mettin, "Jet formation from bubbles near a solid boundary in a compressible liquid: Numerical study of distance dependence," Physical Review Fluids **5**, 093604 (2020), arXiv:2005.05733.
[77]Multidimensional Universal Limiter for Explicit Solution.
[78]S. S. Deshpande, L. Anumolu, and M. F. Trujillo, "Evaluating the performance of the two-phase flow solver interFoam," Computational Science and Discovery **5**, 014016 (2012).
[79]S. M. Damián, *An Extended Mixture Model for the Simultaneous Treatment of Short and Long Scale Interfaces*, Ph.D. thesis, Universidad Nacional Del Litorla (2013).
[80]A. Georgoulas, M. Andredaki, and M. Marengo, "An Enhanced VOF Method Coupled with Heat Transfer and Phase Change to Characterise Bubble Detachment in Saturated Pool Boiling," Energies **10**, 272 (2017).
[81]E. Teodori, P. Pontes, A. Moita, A. Georgoulas, M. Marengo, and A. Moreira, "Sensible Heat Transfer during Droplet Cooling : Experimental and Numerical Analysis," Energies **10**, 790 (2017).
[82]J. Ross MacDonald, "Review of some experimental and analytical equations of state," Reviews of Modern Physics **41**, 316–349 (1969).
[83]I. Chakraborty, "Numerical modeling of the dynamics of bubble oscillations subjected to fast variations in the ambient pressure with a coupled level set and volume of fluid method," Physical Review E **99**, 043107 (2019).
[84]T. G. Leighton, *The Acoustic Bubble* (Academic Press Limited, 1994).
[85]L. Rayleigh, "On the pressure developed in a liquid during the collapse of a spherical cavity," The London, Edinburgh, and Dublin Philosophical Magazine and Journal of Science **34**, 94–98 (1917).
[86]C. E. Brennen, *Cavitation and Bubble Dynamics* (Oxford University Press, 1995).
[87]Mathworks, "MATLAB R2017a,".
[88]J. Rodríguez-Rodríguez, A. Casado-Chacón, and D. Fuster, "Physics of Beer Tapping," Physical Review Letters **113**, 214501 (2014), arXiv:1403.2678.
[89]W. Lauterborn, C. Lechner, M. Koch, and R. Mettin, "Bubble models and real bubbles: Rayleigh and energy-deposit cases in a Tait-compressible liquid," IMA Journal of Applied Mathematics **83**, 566–589 (2018).
[90]T. G. Leighton, "The inertial terms in equations of motion for bubbles in tubular vessels or between plates," Journal of Acoustical Society of America **130**, 3333–3338 (2011).
[91]M. S. Plesset and R. B. Chapman, "Collapse of an initially spherical vapour cavity in the neighbourhood of a solid boundary," Journal of Fluid Mechanics **47**, 283–290 (1971).
[92]E. Maisonhaute, C. Prado, P. C. White, and R. G. Compton, "Surface acoustic cavitation understood via nanosecond electrochemistry. Part III: Shear stress in ultrasonic cleaning," Ultrasonics Sonochemistry **9**, 297–303 (2002).
[93]G. K. Batchelor, *An introduction to fluid dynamics* (Cambridge University Press, 1967).
[94]R. L. Panton, *Incompressible Flow* (Wiley, 1984).
[95]H. K. Versteeg and W. Malalasekera, *An Introduction to Computational Fluid Dynamics* (Longman Scientific & Technical, 1995).
[96]P. Koukouvinis, G. Strotos, Q. Zeng, S. R. Gonzalez-Avila, A. Theodorakakos, M. Gavaises, and C. D. Ohl, "Parametric Investigations of the Induced Shear Stress by a Laser-Generated Bubble," Langmuir **34**, 6428–6442 (2018).
[97]B. Krasovitski and E. Kimmel, "Shear stress induced by a gas bubble pulsating in an ultrasonic field near a wall," IEEE Transactions on Ultrasonics, Ferroelectrics, and Frequency Control **51**, 973–979 (2004).
[98]F. Reuter and R. Mettin, "Electrochemical wall shear rate microscopy of collapsing bubbles," Physical Review Fluids **3**, 25–31 (2018).
[99]R. H. Liu, J. Yang, M. Z. Pindera, M. Athavale, and P. Grodzinski, "Bubble-induced acoustic micromixing," Lab on a Chip **2**, 151–157 (2002).
[100]D. Ahmed, X. Mao, B. K. Juluri, and T. J. Huang, "A fast microfluidic mixer based on acoustically driven sidewall-trapped microbubbles," Microfluidics and Nanofluidics **7**, 727–731 (2009).
[101]S.-W. Ohl and C.-D. Ohl, "Acoustic cavitation in a microchannel," in *Handbook of Ultrasonics and Sonochemistry* (Springer, 2016) pp. 99–135.
[102]E. Zwaan, S. Le Gac, K. Tsuji, and C.-D. Ohl, "Controlled Cavitation in Microfluidic Systems," Physical Review Letters **98**, 22–25 (2007).
[103]S. Li, A.-M. Zhang, and R. Han, "Letter : Counter-jet formation of an expanding bubble near a curved elastic boundary," Physics of Fluids **30**, 121703 (2018).
[104]Q. Wang, M. Mahmud, J. Cui, W. R. Smith, and A. D. Walmsley, "Numerical investigation of bubble dynamics at a corner," Physics of Fluids **32**, 053306 (2020).
[105]D. Kim and D. Kim, "Underwater bubble collapse on a ridge-patterned structure," Physics of Fluids **32**, 053312 (2020).
[106]B. Han, L. Liu, and N. Xiao-wu, "Investigation of the interaction dynamics of a pair of laser-induced bubbles gener-

ated at the same time through double-exposure strobe method and numerical simulations," Physics of Fluids **29** (2017), 10.1063/1.4997081.

[107] J. Mifsud, D. A. Lockerby, Y. M. Chung, and G. Jones, "Data for numerical simulation of a confined cavitating gas bubble driven by ultrasound," (2021), Warwick Research Archive Portal (WRAP), Dataset. `http://wrap.warwick.ac.uk/158721/`.